Mechanical Systems and Signal Processing 134 (2019) 106325

Contents lists available at ScienceDirect

Mechanical Systems and Signal Processing

journal homepage: www.elsevier.com/locate/ymssp

Measurement of slip and separation in jointed structures with non-flat interfaces

Wei Chen [a], Mengshi Jin [a], Iyabo Lawal [b], Matthew R.W. Brake [b,*], Hanwen Song [a]

[a] School of Aerospace Engineering and Applied Mechanics, Tongji University, Shanghai 200092, PR China
[b] Department of Mechanical Engineering, William Marsh Rice University, Houston, TX 77005, USA

ARTICLE INFO

Article history:
Received 3 April 2019
Received in revised form 11 July 2019
Accepted 21 August 2019

Keywords:
Jointed structure
Interface
Kinematic behavior
Nonlinear dynamics
DIC
Slip and separation

ABSTRACT

The nonlinear dynamic behavior and energy dissipation of a built-up structure are often attributable to the contact interfaces between the subcomponents of the structure. Due to the lack of direct measurement techniques for jointed interfaces, the local kinematic behaviors inside the interfaces are not well understood. Additionally, the part-to-part variability of the interface (such as surface curvature, surface roughness, geometric features, and residual stress) significantly affects the structural dynamics and, therefore, introduces uncertainty in the measured response of a jointed structure. In this paper, the local kinematic behavior of a jointed interface is measured by digital image correlation (DIC) during shaker excitation at the first two resonant frequencies for 10 different perturbations of the same assembled structure. For these perturbations, the interface curvature is varied to represent typical manufacturing variations. Experimental validation shows that the DIC method is able to measure slip and separation in the interface with a resolution of up to 0.23 μm for the reported experiments. Additionally, the nonlinear properties of the system are characterized via impact hammer test. For the first mode of the structure, separation (clapping) and microslip behaviors are observed; additionally, for the second mode, macroslip motions are observed. These results challenge multiple assumptions prevalent in the modeling of jointed structures.

1. Introduction

Mechanical joints are known to be a source of nonlinearity, and considerable energy dissipation, in built-up structures [1]. The nonlinear nature of the interfaces, both in terms of stiffness and dissipation, originates in a complex set of interactions between the two interfaces. These interactions, because they are internal to the joint, have not been previously measured in detail. Consequently, the mechanics of jointed interfaces are poorly understood. Directly measuring the physics of joints is challenging since the main interactions take place within the interface of the joints, where sensors cannot be placed without changing the behavior of the joint. Without a better understanding of the physical mechanisms that dissipate and transfer energy across a joint, it is prohibitively challenging to develop a predictive model of joints to match the experimentally observed behavior and to guide the design of future jointed structures. Further, it is unknown how much information is needed to predict the response of a jointed structure. For instance, due to manufacturing, there is significant part-to-part variability (e.g. surface roughness, meso-scale curvature, macro-scale geometry, and residual stress), which can span from

* Corresponding author.
E-mail address: brake@rice.edu (M.R.W. Brake).

https://doi.org/10.1016/j.ymssp.2019.106325
0888-3270/

the nano-scale to the macro-scale. Even using state-of-the-art techniques to develop calibrated models of jointed structures, these models are unable to match the responses of more than the first few modes of a structure [2]. This motivates the question: what are the primary contributors to the discrepancies between models and experiments?

Over the last two decades, extensive research has concentrated on modeling and predicting the dynamics of a jointed structure [3–7]. There have been multiple approaches to this modeling challenge. A low fidelity modeling approach for a joint is a linear system, with two linear subcomponents connected by linear springs and dashpots. Due to the linear model characteristics, the model cannot reproduce the experimentally observed nonlinear phenomena (such as resonance shift, damping change, and mode coupling, etc.), nor accurately describe the mechanism for energy dissipation [8]. To develop a nonlinear model of a system, the framework proposed by [9] begins with a linear model, then identifies the source of nonlinearity and characteristics of the nonlinearity from experiments before introducing an appropriate nonlinear model into the previously linear system. Thus, a common way to model a joint is as two linear substructures connected by a few nonlinear elements composed of a parallel or series arrangement of springs, dashpots, and Coulomb sliders. However, this kind of modeling method only fits the nonlinear characteristics of the system, not the mechanical sources of the nonlinearity. As an example, a detailed finite element model applies forces in a nodal sense or integrated over an element, and the nonlinearity is introduced by a Coulomb friction model that is typically applied as a point-wise force. In reality, though, friction acts continuously over an area with some distribution of asperities and other tribological features. Additionally, the well-known Coulomb slider breaks down when used to describe the frictional energy dissipation and is unable to capture both macroslip and microslip effects accurately within the same model [10].

An alternative approach to model the interface is proposed by Segalman [11], in which all of the interface degree-of-freedoms (DOFs) on each side of the interface are tied to a single DOF rigidly. A constitutive model (the four-parameter Iwan model) that is designed to represent the hysteretic properties of a jointed structure is used to connect the two DOFs (one from each side of the interface). The single DOF model replaces the kinematics of the adjacent surfaces with a nonlinear constitutive model, which is capable of capturing joint behavior over both the microslip and macroslip regimes. The whole interface can also be divided into several patches to represent complex dynamic behavior [2]. The constitutive parameters of the model are typically calibrated for representative experimental data. Further, with the assumption of weakly nonlinear response and uncoupled modes, a modal Iwan framework was proposed to model the amplitude-dependent properties of each mode of a jointed structure independently [12,13]. These approaches, thus, sacrifice the fidelity of the joint's physics while attempting to match the hysteretic behavior of the joint in some regimes of excitation.

In contrast to the classic Iwan model implementation [10], typical high fidelity models connect the nodes on two sides of an interface with Jenkins or 3D contact elements [14]. This modeling method has the potential to simulate the complex nonlinear dynamic behavior of the interface. However, it cannot predict the amplitude-dependent properties (and thus hysteresis) accurately without calibration. Since thousands of the nonlinear DOFs are introduced in the model, the calculation and calibration are time-consuming. Zero-thickness elements [15] and thin-layer elements [16] are also high fidelity modeling methods for the contact interface. Parallel research to the present work has shown that by implementing an interface model that is consistent with what is measured here, it is possible to blindly predict (without calibration) the response of a jointed structure with less than 2% error [17]. However, it is still not clear as to how the parameters for the constitutive models may be estimated for a fully predictive model.

Despite the strengths of these modeling methods, there are many assumptions in the modeling approaches that violate physical reality. For the four-parameter Iwan model, since this patch modeling is rigidly connected between the master node and the nodes in the patch, the same frictional force is applied to all nodes within the contact patch. With this assumption, the nodes in the same patch have the same motions (constant contact area) and pressure distributions. Furthermore, this modeling method is incapable of reproducing the local interfacial physics (kinematics). The local kinematics include the relative tangential and normal motions with some distribution at the interface. Though the slip behavior is widely considered by many models, the dynamic effect of the clapping of the two contact patches is generally neglected in modeling. Additionally, it is well accepted that microslip constitutes the bulk of the energy dissipation of a joint, but the relative contribution of clapping in energy dissipation is unknown [18].

Many assumptions for the kinematic behaviors of the interfaces under the dynamic excitations have been shown to be invalid by recent experimental studies. For the modeling, the normal forces (pressures) acting on contact patches in the interface are often assumed to be constant, and that the two contact patches are always in contact. Recent experimental and numerical studies have highlighted that the contact patch dynamically evolves over a period of excitation [17,19–21]. Using an electronic pressure film system, the contact pressure in the interface can be measured during dynamic excitation [17,20,21]. The results showed that the contact pressure and contact areas vary periodically during the dynamic excitation, both at the edges of the interface where clapping behavior was observed and near the center of the interface, where the contact pressure fluctuated up to 10% during a period of excitation. The transient evolution of the contact patch under impact testing was studied in [21] using a similar pressure film, in which the interfacial contact pressures and the contact area inside a bolted lap joint were measured. The variation of the contact pressure and area implies that the separation of contact surfaces occurs during impact responses. Since the contact pressure measurements are limited to sampling frequencies below 1 kHz, and also physically change the interface, a new approach is needed to gain further insight into the interface dynamics.

Digital image correlation (DIC) is a promising approach for making the full-field measurement of a dynamic system [22]. Previously, most DIC research focused on studying linear systems (e.g., [22]); however, recently Klaassen et al. [23]

demonstrated that it was possible to measure the normal kinematics of a jointed interface. Specifically, the separation behavior of the interface at the first three modes under steady sinusoidal motion was extracted with high spatial resolution. The results from [17,20,21,23] indicate that several commonly held assumptions for modeling jointed structures may be invalid. These assumptions include that contact pressure is constant under the frustum of the bolt, and that there is no dynamic impact internal to the interface. When coupled with the findings of the numerical study of [24], there is, perhaps, a significant and far-reaching ramification: in order to be predictive, interface models must be improved to capture the local kinematics of the interface. These investigations [17,20,21,23,24] have raised several questions pertinent to the dynamics of jointed structures. In particular, more information is needed on not only the normal behavior of the interface (as mentioned in [17,20,21,23]), but also on the tangential behavior of the interface, which has not been previously measured at a sufficient resolution. This paper seeks to both measure the normal and tangential behavior within an interface and to use other experimental techniques to gain new insights into the dynamic jointed structures.

Any information regarding how the contact patch evolves during dynamic excitation would be able to provide crucial insights to modeling. Towards a better understanding of the local kinematics of the joints, this research focuses on experimentally measuring the slip and separation behaviors of interfaces through DIC. Both the amplitude-dependent properties and the kinematic behaviors of different interface configurations were experimentally studied, where the amplitude-dependent natural frequencies and damping ratios were extracted from impact testing, and then the kinematic behaviors were recorded under steady-state excitation of each mode. Details about the experiment design, the test specimens, and data processing in both impact and shaker testing are presented in Section 2. In Section 3, the results of the amplitude-dependent natural frequencies and damping ratios, and of the local kinematics (slip and separation behaviors) for the test specimens are summarized. The slip and separation behaviors for different interface configurations are compared and discussed. In Section 4, the ramifications of the experimental observations for modeling are discussed. Finally, the conclusions are given in Section 5.

2. Methodology

The overview of the experimental methodology is shown in Fig. 1, including assembly, pre-experiment hammer test, step sine test, fixed sine test, and post-experiment hammer test. The test system and assembly process are described in Section 2.1. The hammer tests were conducted to measure the dynamic characteristics of the system before and after the fixed sine test (see Section 2.2) in order to assess how much the system changed due to damage incurred from the fixed sine testing [25]. To identify the natural frequencies of each structure at a certain force level, a step sine test was conducted with the step size of 0.1 Hz about the first and second resonances. Once the natural frequencies were identified for a force level, the structure was excited by a fixed sine at the prescribed frequency and force level. Throughout the fixed sine testing of the systems, the natural frequencies of the first and second mode typically changed by 0.8 and 2 Hz respectively as the shaker amplitude was increased from 2 N to 5 N due to the nonlinearity of the joint. The high-speed camera was employed to capture the motion of the interface, and the DIC method was used to post-process the photos to get the displacement of the interface, which is shown in Section 2.3. To verify the accuracy of the DIC measurement, the verification experiment was conducted and shown in Section 2.4.

2.1. Test system

To study the slip and separation behaviors of jointed structures, multiple specimens with different interface curvatures are studied. Previous experiments have shown that the part-to-part variation of jointed structures can have a significant influence on the dynamic behavior [25]. In particular, the meso-scale curvature of a structure that results from the

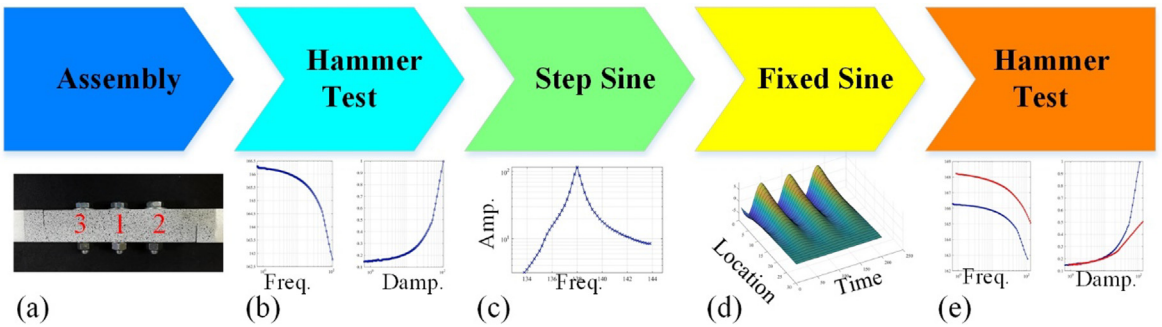

Fig. 1. The procedures for the experimental study include the (a) assembly process for jointed structures, (b) hammer tests before the fixed sine test to obtain the amplitude-dependent natural frequency and damping ratio, (c) step sine tests for searching the amplitude-dependent natural frequencies, (d) camera recording the responses of the jointed interface during the fixed sine tests, and (e) hammer tests after the fixed sine tests to compare the frequency and damping with ones from before the fixed sine test.

manufacturing process (such as machining patterns or a non-flat curvature) can change the natural frequencies of a jointed structure by up to 30% and the damping ratios by an order of magnitude [25,26]. To investigate the effect of typical manufacturing variations, the standard Brake-Reuß Beam (BRB) [25] and its variations with different curvatures were used in this experiment. The standard BRB contains a three bolt lap joint and was manufactured using wire electrical discharge machining. Its geometric parameters can be seen in Fig. 2(a) and (b) and more details about the BRB can be found in [1].

To ensure the consistency and repeatability of the experiment, BRBs were assembled according to the method outlined by [27]. A constant gap was maintained using a 0.35 mm thick shim along the edges of the beam halves to ensure accurate alignment of the interface. The beam halves were bolted together with three stainless steel 5/16″-24 bolts, where the torque for each bolt was 19.6 N · m. The bolts were first tightened to 70% of the desired torque level in the order shown in Fig. 1(a), and then to the full level in the same order. Following the bolt tightening procedure, the alignment shim was removed.

In addition to the standard BRB, the multiple permutations of the BRB with non-flat interface were investigated in this research. Specifically, four different interface curvature heights (0, 250, 1000, and 5000 μm) were manufactured by changing the peak distance in the vertical direction at the midline of the jointed interface (as shown in Fig. 2(c)). To identify the combinations of the beam halves, three major categories were defined according to previous work [26]: conformal configuration, edge gap (EG), and center gap (CG). For the conformal configurations, the convex and concave interfaces with the same height were joined together (see Fig. 2(d)), and for the EG and CG cases, the flat interface was joined with convex and concave ones (see Fig. 2(e) and (f)), respectively. The full set of systems studied is given in Table 1.

The test specimens are shown in Fig. 3(a), where the 250 μm curvature is a realistic manufacturing defect and the 5000 μm is an extreme case used to study the effect of the curvatures. The test beam was suspended (0.88 m) using fish lines to simulate a free-free boundary condition. The system was excited by a 267 N modal shaker connected to the beam via a stinger (see Fig. 3(b)), which was controlled via an open loop control scheme using a 22.29 mV/N force transducer connected at the stinger location. The response of the system was also recorded via two accelerometers, located at the shaker attachment point and 12.5 cm from the opposite end of the beam (as shown in Fig. 2(b)), with sensitivities of 97.7 and 104.7 mV/g respectively. These accelerometers were used to capture the ringdown response of the system in the impact hammer experiments.

2.2. Impact hammer test

Before the DIC measurements for each combination of the beam halves, a hammer test was conducted to show the nonlinearity of these structures. The impact position of the hammer was the same as the shaker attachment point (see Fig. 2(b)). The beam was impacted at 500 N, and the force and acceleration responses were sampled at 8192 Hz for 4 s. To assess the repeatability of the impact measurement, multiple tests were conducted: two at 500 N (shown in the following results), two at 300 N (not shown), and two at 100 N (not shown). From each impact test, the response of a single mode (Fig. 4(b)) was extracted from the raw acceleration data (Fig. 4(a)) by: reversing the time signal and then using a 4th-order Butterworth band pass filter (with bandwidth of 60 Hz) [28,29]. The frequency domain response of the filtered response and raw data are shown in Fig. 4(c). The Peak Finding and Fitting (PFF) method [29] was then used to extract the instantaneous damping and frequency of the system, as shown in Fig. 4(d) and (e).

As shown in Fig. 4(d), the natural frequency decreases about 0.7 Hz with the increase of the response amplitude from 0.5 to 9.5 $m \cdot s^{-2}$, which illustrates the 'softening' characteristics of jointed structures as they transit from being fully stuck at low

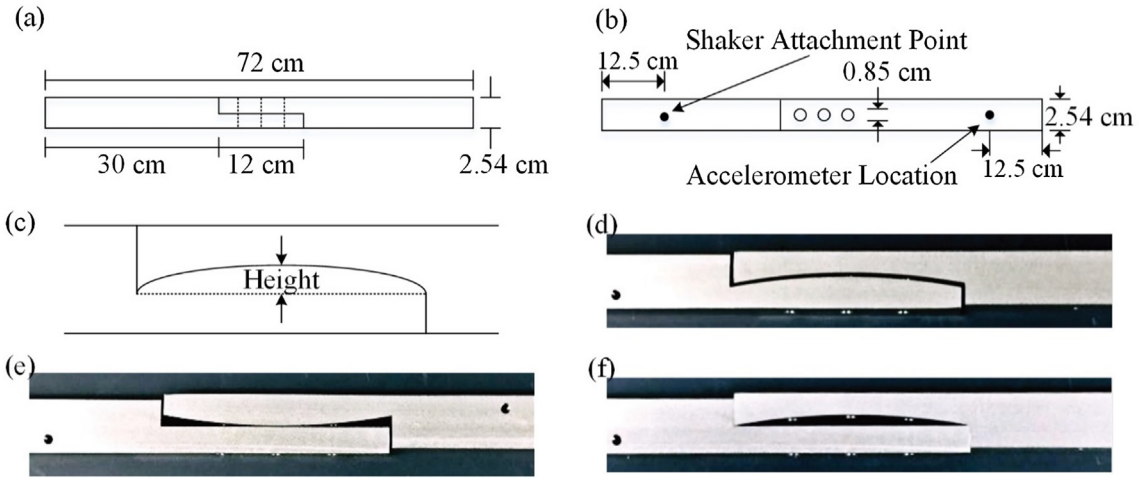

Fig. 2. The geometry of the BRB as seen from the (a) top and (b) side, (c) the definition of the curvature height, (d) the 5000-5000 conformal assembly, (e) the 0-5000 EG assembly, and (f) the 5000-0 CG assembly.

Table 1
The combinations of beam halves used in the test. unit (μm).

Conformal	EG	CG
0-0	\	\
250-250	0-250	250-0
1000-1000	0-1000	1000-0
5000-5000	0-5000	5000-0

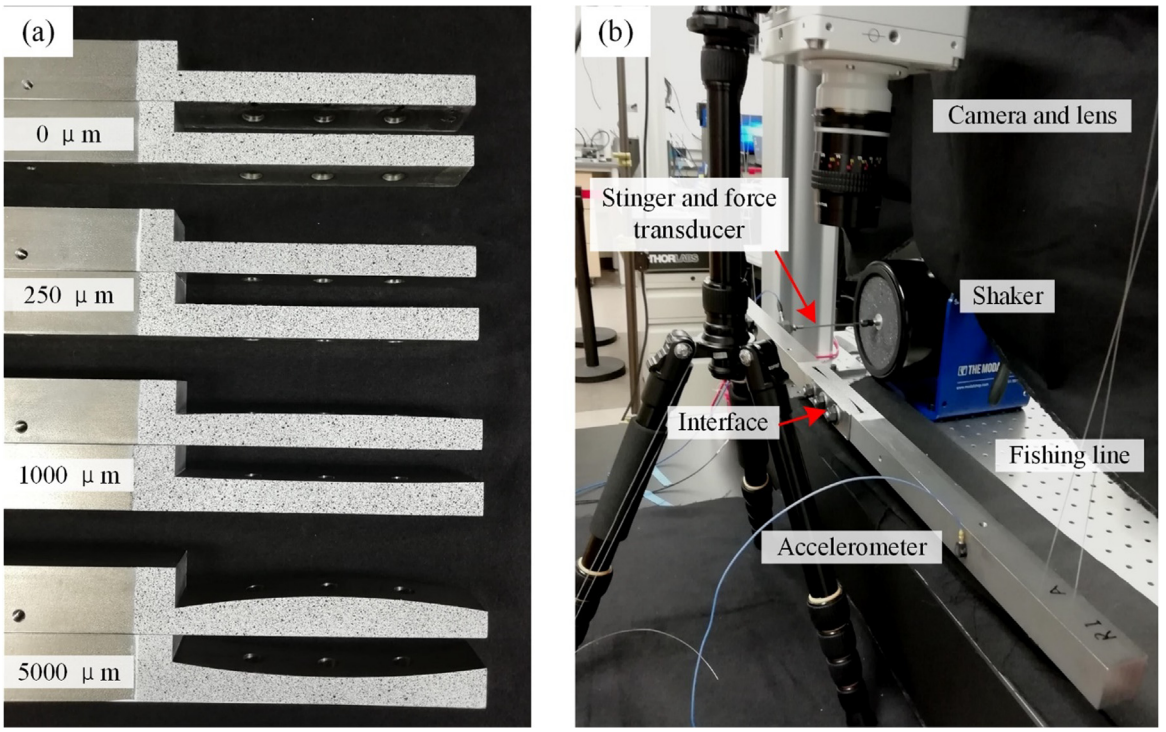

Fig. 3. Test structures and experimental setup for the DIC measurements. (a) Beams used in the experiment, including the speckle pattern used in the DIC measurements. (b) Experimental test setup for the DIC measurements.

amplitudes to slipping (at least partially) at higher amplitudes. Once the entire interface is in a state of slip, the frequency response converges to a lower natural frequency associated with the fully slipping condition (not achieved in Fig. 4). For the damping ratio, the capacity of the interface to dissipate energy increases with response amplitude as more of the interface transits from being stuck to partly sliding (termed microslip in the joints community [1]). Consequently, a significant increase in damping ratio is observed until the macroslip threshold, in which the entire interface is sliding, is reached; however, this response level is not reached in these experiments. Similar properties can be observed using a Hilbert transform method too [27,30,31]. To show the variation of the dynamic features of the beams, the hammer test was conducted after shaker testing to compare with the pre-shaker results.

2.3. Step sine testing

According to the natural frequencies obtained from the impact hammer testing, the force-controlled step sine was conducted around the frequencies of the target modes. The force level of the testing was set as 2 and 5 N with a frequency step of 0.1 Hz. The accelerometer was placed at the same location as the hammer test, more details can be seen in Fig. 3(b). The sampling frequency was set as 8192 Hz and the beam was excited for 6 s to obtain a steady-state response for each frequency step. The response amplitude at each step was recorded to find the natural frequency, which corresponds to the highest response level. An example of step sine testing with force levels of 2 and 5 N for the first mode is shown in Fig. 5. With the force level increasing from 2 to 5 N, the natural frequency decreases from 151.3 to 150.7 Hz. In addition, the measured peaks are not symmetric and are both skewed to the left, which is further indicative of softening behavior.

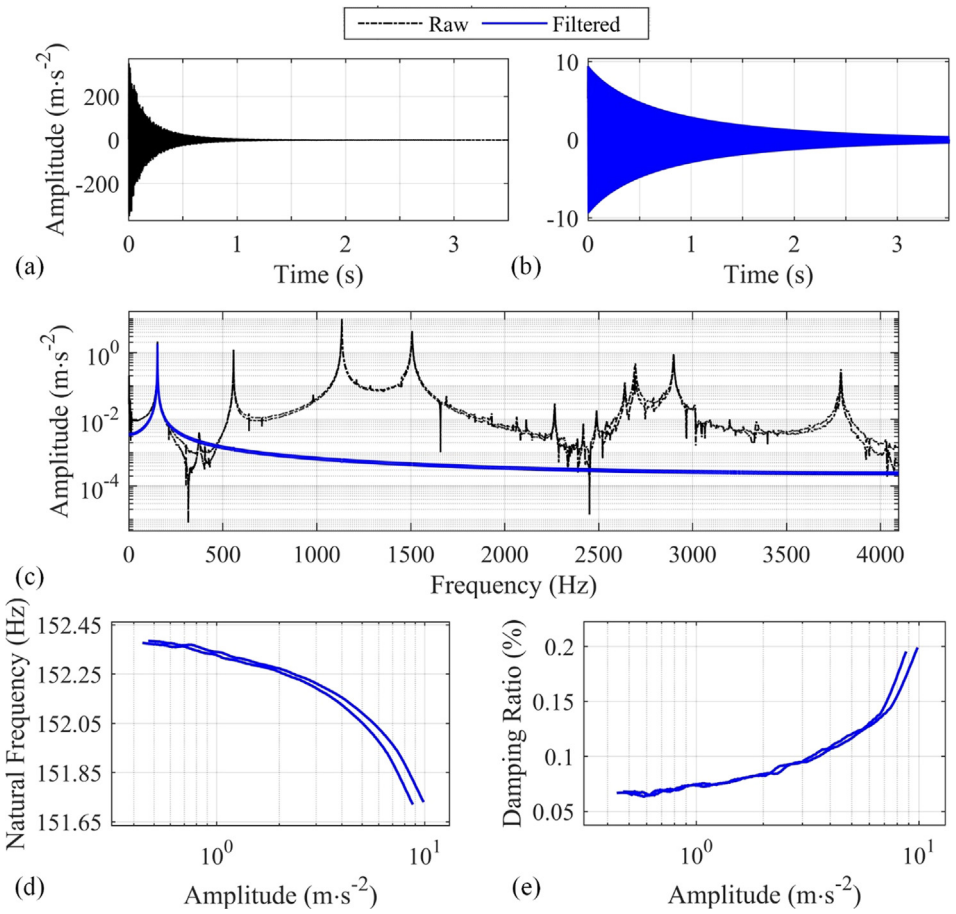

Fig. 4. The post-processing process for the hammer tests, shown are (a) the raw data from the accelerometer, (b) the band pass filtered responses in time domain, (c) FFT of the raw data from the impact testing and the band pass filtered responses, (d) amplitude-dependent natural frequency, and (e) amplitude-dependent damping ratio. The two band pass filtered responses shown in each plot are from the two 500 N impact hammer tests for the beam with the flat interface.

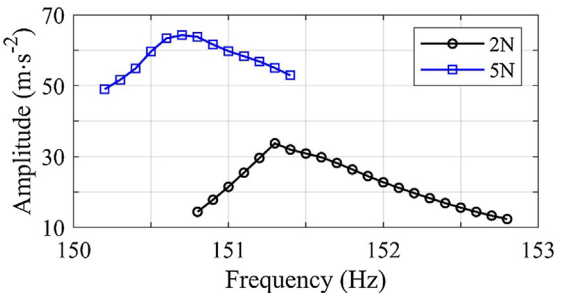

Fig. 5. The response amplitude of the beam with the flat interface during the step sine testing with constant force levels of 2 and 5 N for the first mode.

2.4. DIC test

During shaker testing, DIC is used to measure the displacements of the interface. DIC is a class of non-contact methods that acquire images of an object, and performs image analysis to extract the full-field shape, deformation, and/or motion of the object [32–34]. The jointed interfaces of the beams were painted with white matte paint and then black ink was sprayed on the surface to make the random speckles that the DIC method tracks. The recorded photos were processed by the DIC software 'Digital Image Correlation Engine' (DICe) [35] to extract the displacement of the interface. The DIC method works by creating overlapping square windows (or subsets) on the area of interest and tracking the motions of the subsets via

image correlation. The displacement responses extracted by image correlation are the average responses of the subsets, which are commonly referred to as the responses at the center points. For a higher spatial resolution in the measurements, a smaller subset size is desirable; however, smaller subset sizes will bring about uncertainty during the image correlation and may cause more error for the extracted responses [36]. In the experiment, the length of the subset was set as 35 pixels (as each subset is square, this results in a total of 1225 pixels inside the subset: $35 \times 35 = 1225$) and the overlap between two subsets was 18 pixels (shown in Fig. 6). The purpose of the study is to measure the motions of the interface. Therefore, the measurement points should be as close to the interface as possible. However, when the subsets had overlap with the interface, the measurement may fail since there was significant relative motion inside the subset. Considering that the subsets should be close to the interface and not include the interface itself, the subsets just above and below the interface were selected to be tracked. In Fig. 6, the subsets in red (top) and blue (bottom) were selected for DICe to calculate the displacement along these lines. For more details on establishing a good DIC experiment, see [34,37].

To improve the resolution of the measurement, a 55 mm lens was used and the jointed interface was divided into 3 regions: left, right, and center. The resolution for the left and right regions was 1024×512 pixels, and the resolution for the center region was 1152×424 pixels. The frame rate for all tests was set as 10,000 frames per second. For each beam, a total of eight to twelve experiments were performed: the system was excited at two different levels (2 N and 5 N) and two different frequencies (the first and second resonant frequencies), and three measurements were made for each condition – the left portion of the interface, the center portion, and the right portion. The responses of the subsets of pixels above and below the interface were extracted, including the tangential (X direction) and normal motions (Y direction). The relative motion in the X and Y directions between the top and bottom sides of the interfaces was then calculated. Since the beam was excited by a fixed sinusoid, a 4th-order Butterworth band pass filter can be employed to decrease the effect of environmental noise (such as from the camera's fan's vibration, air currents within the lab, etc.).

2.5. Verification

In order to validate the accuracy of the DIC method for the measurement of the displacements of the interface during excitation, an experiment was performed to compare the results with other well-developed methods (i.e., laser Doppler vibrometer (LDV) and accelerometers). The BRB with a flat interface was used in the verification experiment, and an accelerometer was mounted at the right side of the interface. A LDV was used to measure the position adjacent to the accelerometer, which can be seen in Fig. 7(a). The resolution of the camera was 1024×512 and the frame rate was 10,000 frames per second. Fig. 7(b) shows a photo from the camera, where the DIC subset for measuring was selected close

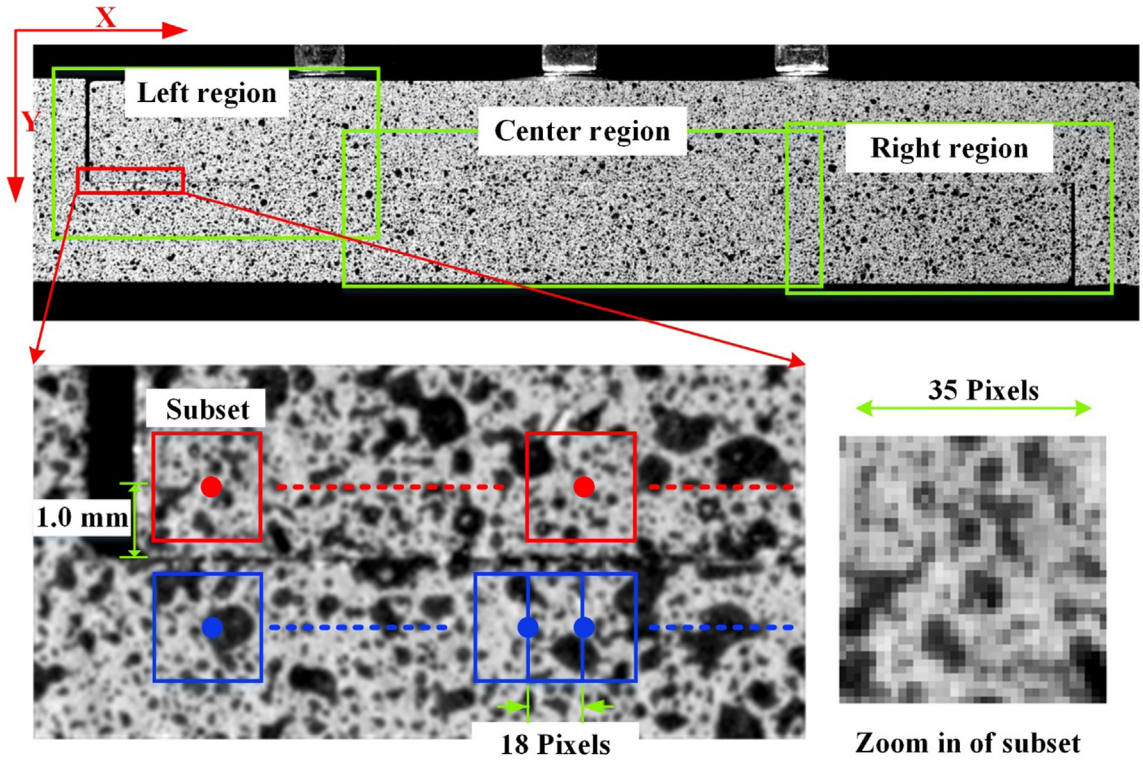

Fig. 6. Details of the DIC measurement strategy for the jointed interfaces.

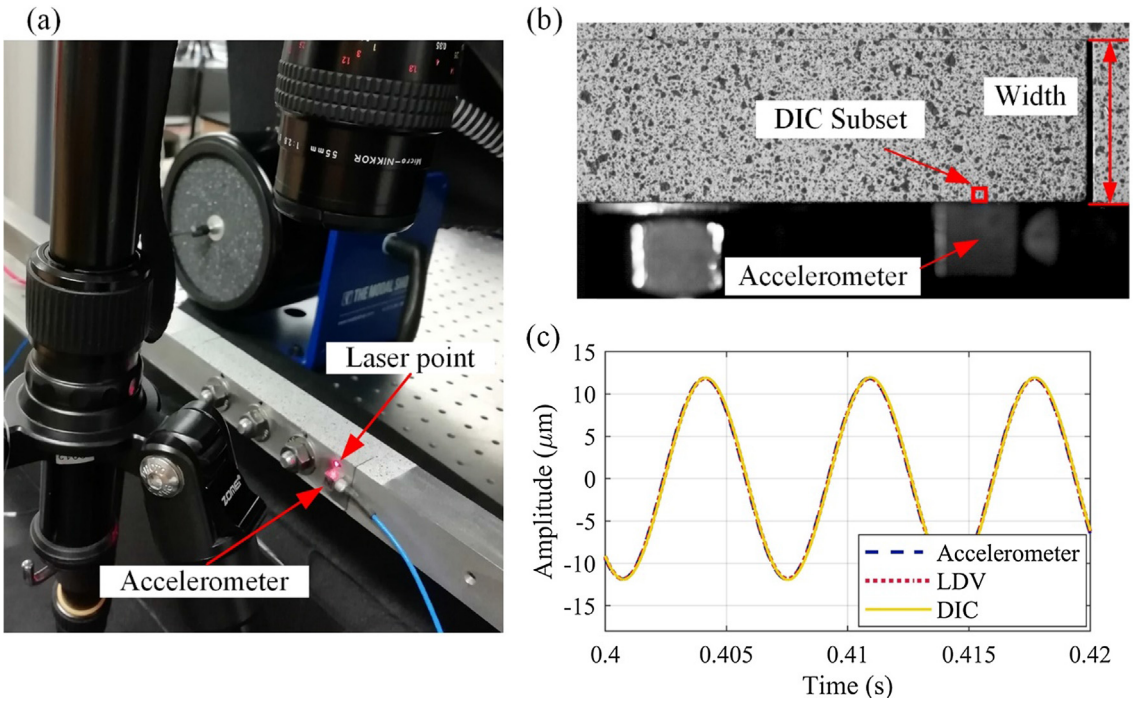

Fig. 7. Verification experiment for the DIC method. (a) Photo of the experimental setup, (b) sample photo from the camera, and (c) time history responses of all three methods.

to the edge of the beam, by the accelerometer location. The beam was excited at 147.3 Hz (the first mode) and 551 Hz (the second mode) at three different force levels. The sampling frequency of the accelerometer and LDV was 8192 Hz.

To directly compare the time history response against the displacements derived from the DIC method, the velocity response from the LDV was numerically integrated one time, and the acceleration signal was numerically integrated twice. The numerical integration brought about low-frequency contamination in the signals, which was filtered via a 4th-order Butterworth band pass filter. For the in-plane motion measurement, an object with known dimensions in the image can be a reference dimension to convert the measurements from units of pixels to those of physical units. The width of the beam (Fig. 7(b)) was selected as the reference dimension and the conversion factor in this experiment was the width of the beam (in physical units of μm) divided by the number of pixels that it spanned in the image. The measured displacement from the DIC method was then converted to units of μm by multiplying by the conversion factor (39.31 μm/pixel in this test).

The beam was excited for 20 s to the reach steady-state vibration. The accelerometer and LDV recorded the response of the whole process, while the camera only recorded the steady-state responses for 2 s (due to limited memory). Fig. 7(c) shows the steady-state time histories of these three methods. The acceleration and velocity responses were sampled synchronously by a Siemens LMS data acquisition system. However, the time synchronization was not possible between the camera and LMS system. Therefore, the time series of the DIC responses were aligned manually with the other two methods for the last 2 s with respect to the phase of the steady state response. Since the excitation was a fixed sine, the amplitudes of these signals can be compared with each other without suffering the effect of the synchronization. Table 2 shows the amplitude results of the three measurements.

As seen in Table 2, the response measured with all three techniques is within 0.6 μm of each other. The largest relative error for measurements of mode 1 is less than 1.0% (corresponding to a displacement of 0.57 μm for the high amplitude excitation of the system), and for mode 2 is approximately 3.0% (corresponding to 0.1 μm difference for the medium amplitude

Table 2
Comparison of the response peaks from different methods. Amplitude unit (μm).

Method	Low		Medium		High	
	Mode 1	Mode 2	Mode 1	Mode 2	Mode 1	Mode 2
Accelerometer	11.86	0.8152	48.04	3.311	87.01	16.96
LDV	11.84	0.8254	47.91	3.347	86.58	16.89
DIC	11.91	0.8150	47.88	3.415	86.44	16.66
Error between Accelerometer and DIC	−0.42%	0.02%	0.33%	−3.05%	0.66%	1.80%
Error between LDV and DIC	−0.59%	1.27%	0.06%	−1.99%	0.16%	1.38%

Table 3
Low amplitude properties of modes 1 and 2 prior to the fixed sine testing for all configurations.

Configuration	Curvature combination	Low amplitude f_1 (Hz)	Low amplitude ζ_1 (%)	Low amplitude f_2 (Hz)	Low amplitude ζ_2 (%)
Conformal	0-0	152.3	0.06	557.0	0.04
	250-250	166.3	0.14	574.2	0.06
	1000-1000	172.5	0.21	582.8	0.09
	5000-5000	170.8	0.13	581.4	0.08
EG	0-250	138.4	0.05	541.5	0.05
	0-1000	125.0	0.04	529.6	0.02
	0-5000	120.7	0.08	512.3	0.02
CG	250-0	182.0	0.08	592.7	0.05
	1000-0	182.2	0.05	587.6	0.04
	5000-0	185.5	0.03	572.0	0.02

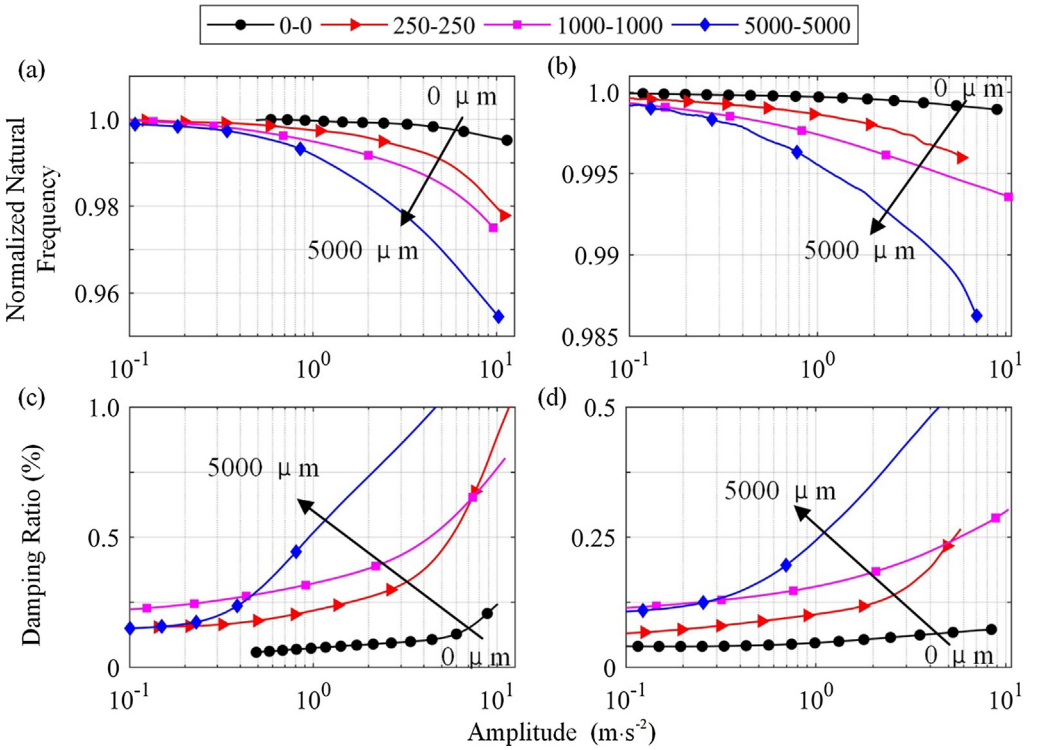

Fig. 8. The amplitude-dependent natural frequencies ((a) and (b)) and damping ratios ((c) and (d)) for the first ((a) and (c)) and second ((b) and (d)) modes of conformal configurations from the hammer tests of 500 N. The natural frequencies are normalized with respect to the linear natural frequency for each system.

Table 4
The changes of the damping and natural frequencies from before to after fixed sine testing.

Configuration	Curvature combination	Change f_1 (Hz)	Change ζ_1 (%)	Change f_2 (Hz)	Change ζ_2 (%)
Conformal	0-0	**+0.5**	**−0.19**	−0.1	−0.03
	250-250	**+1.9**	**−0.53**	**+2.2**	**−0.14**
	1000-1000	**+0.8**	−0.04	**+0.7**	0
	5000-5000	**+2.5**	**−0.34**	**+2.2**	−0.07
EG	0-250	**−0.5**	**−0.26**	**−0.7**	−0.03
	0-1000	+0.1	−0.05	−0.1	0
	0-5000	+0.1	0	0	0.01
CG	250-0	**+2.0**	**−0.46**	**+1.3**	−0.03
	1000-0	0	−0.04	−0.2	0
	5000-0	0.1	−0.05	+0.3	−0.01

The bold numbers indicate large changes in the system properties (i.e. of 0.5 Hz or 0.1% damping).

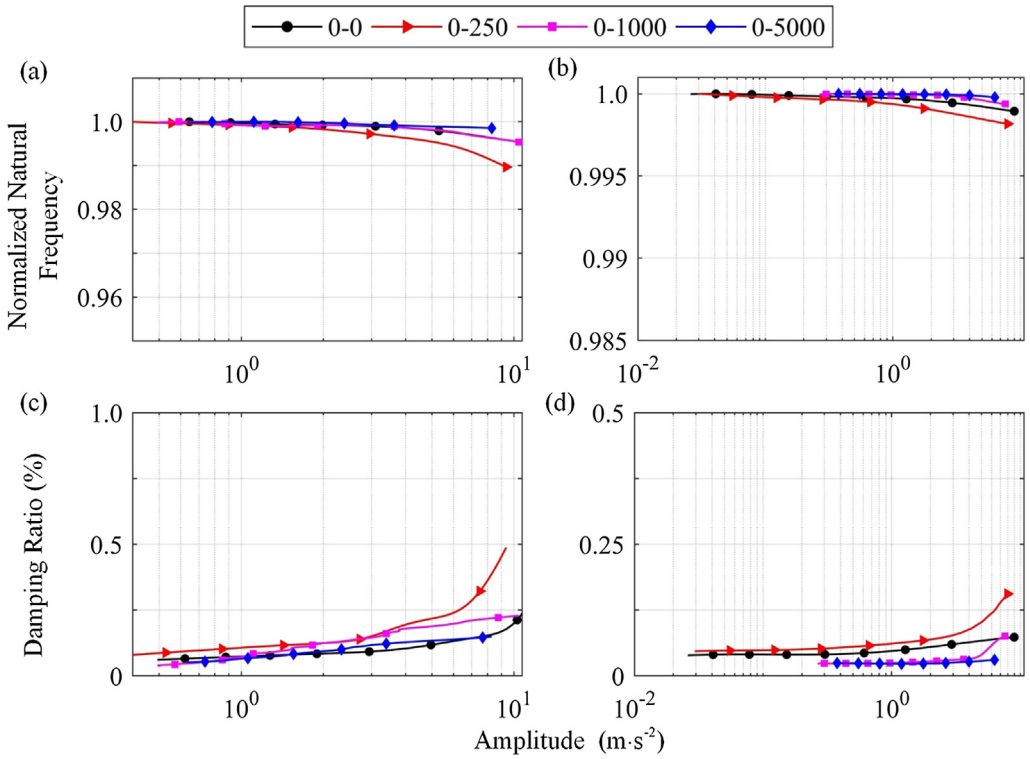

Fig. 9. The amplitude-dependent natural frequencies ((a) and (b)) and damping ratios ((c) and (d)) for the first ((a) and (c)) and second ((b) and (d)) modes of EG configurations from the hammer tests of 500 N. The natural frequencies are normalized with respect to the linear natural frequency for each system.

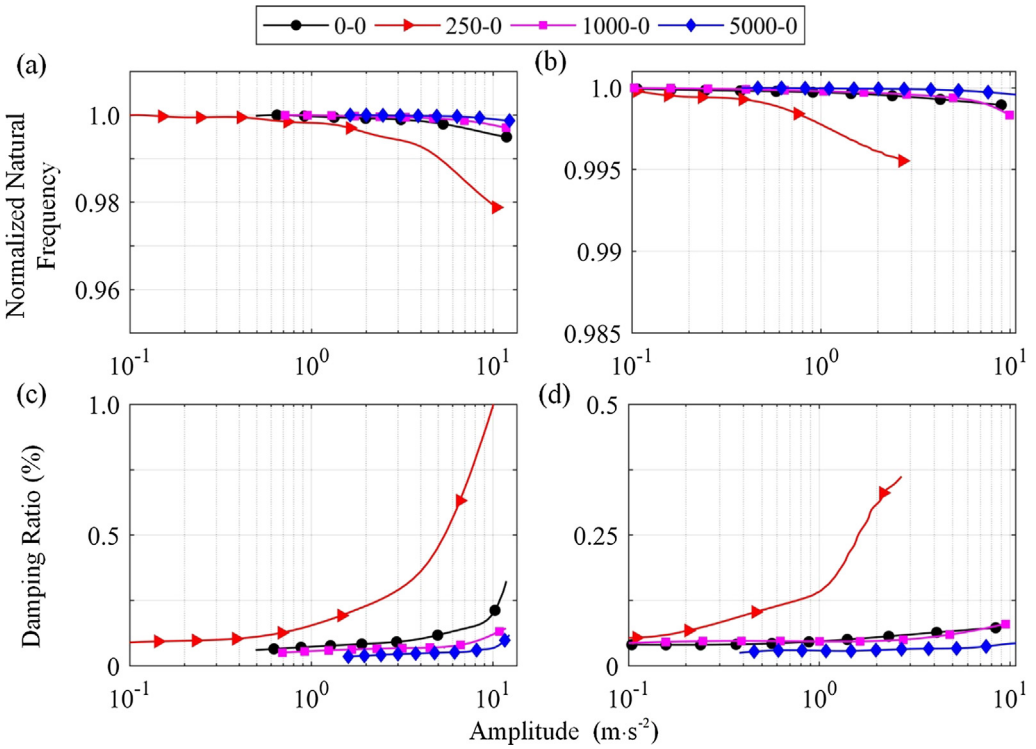

Fig. 10. The amplitude-dependent natural frequencies ((a) and (b)) and damping ratios ((c) and (d)) for the first ((a) and (c)) and second ((b) and (d)) modes of CG configurations from the hammer tests of 500 N. The natural frequencies are normalized with respect to the linear natural frequency for each system.

excitation). It is worth noting that in several cases the LDV and DIC show higher agreement than the accelerometer and DIC. This could partly be attributable to the accelerometer data needing to be integrated twice to calculate the displacement of the system for direct comparison with the DIC data. The largest difference between LDV and DIC is within 0.23 μm. This gives confidence that the DIC measurements in this situation are accurate to their noise floor of 0.006 pixels (approximately 0.23 μm).

3. Results

3.1. Hammer tests

Hammer tests were conducted before and after each series of experiments to both quantify the nonlinearity of the test structures and to assess the wear caused by shaker testing. For all hammer tests, the procedure described in Section 2.2 is followed. The low amplitude properties in Table 3 are taken from the lowest amplitude extracted via the PFF method for each experiment. While the lowest amplitude itself varied from test to test, all measurements appeared to converge to a 'low amplitude limit,' which is typically considered the linear response of the system. The amplitude-dependent properties (natural frequency and damping ratio) measured from the hammer tests of the conformal systems before the fixed sine tests are shown in Fig. 8. The amplitude-dependent natural frequencies are all normalized by the low amplitude natural frequencies.

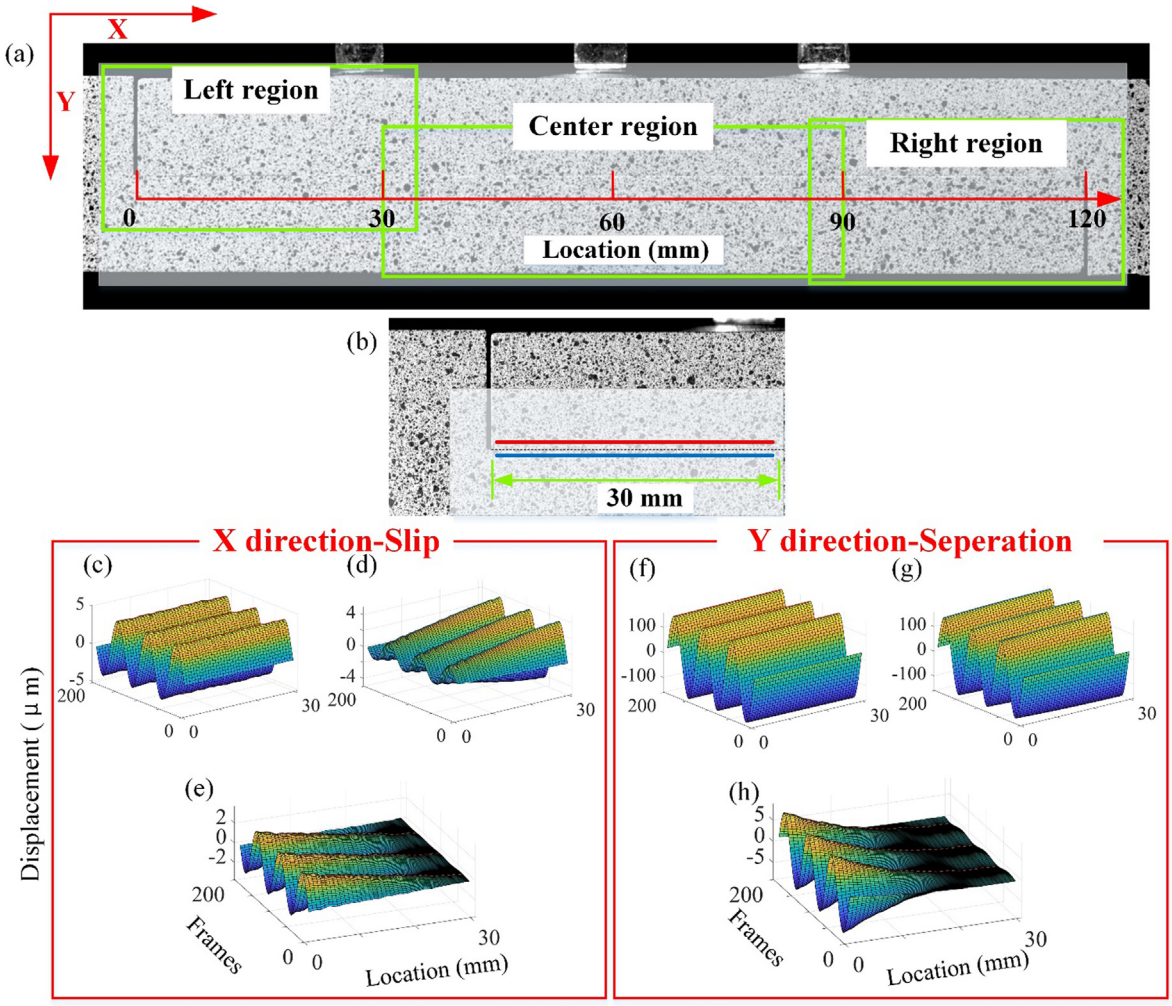

Fig. 11. The process to extract the relative motions in the X and Y directions. Shown are (a) the whole interface of the BRB with the flat interface, (b) a photo of the left region of the interface from which the responses of the red and blue lines are extracted, (c) and (d) the displacement time histories of the red and blue lines, respectively, in the X direction, (f) and (g) the displacement time histories of the red and blue lines, respectively, in the Y direction, and (e) and (h) the response difference between red and blue lines in the X and Y directions, respectively.

The results of Table 3 can be explained from analyzing the contact stiffness of the different geometries tested. From the derivation of Hertz's model for contact mechanics [38], when the assumptions in this model are revised to investigate pin-in-hole contact (which is similar to the conformal configuration in this study), the contact stiffness is up to 25% greater than for Hertzian contact [38] (which is the same type of contact exhibited by the EG condition). Further, for the conformal configuration, the contact area is directly related to load, resulting in a large portion of the interface that is in microslip over each period of vibration and thus leading to a higher damping ratio. For the CG condition, contact in the interface is restricted to two narrow strips at the extremities. As a result, the contact pressures are much higher, and, consequently, the forces nec-

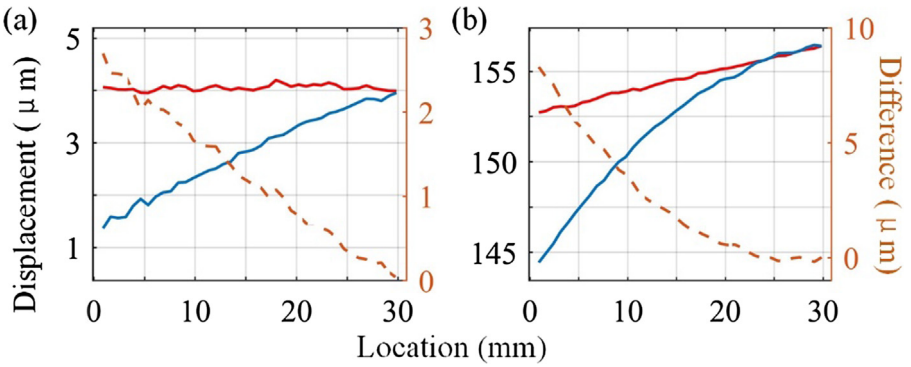

Fig. 12. The amplitudes of the slip and separation behaviors of the left region along the interface. Shown are the response amplitudes of the red line, blue line and their difference in the (a) tangential and (b) normal directions. The solid red and blue lines represent the responses above and below the interface, respectively. The dashed orange line shows the difference between the red and blue lines. The y-axis on the left side is the amplitude of the responses. The y-axis on the right side is for the difference of the responses. (For interpretation of the references to colour in this figure legend, the reader is referred to the web version of this article.)

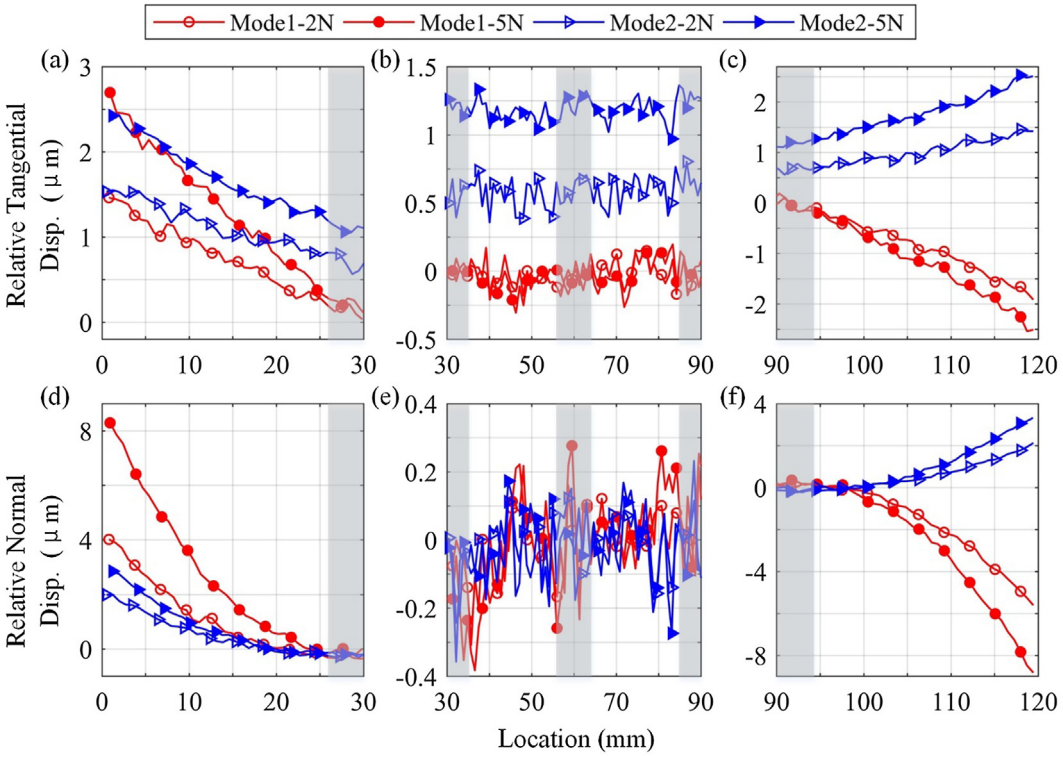

Fig. 13. The relative tangential and normal displacement across the entire interface for excitation levels of 2 and 5 N and excitation frequencies at the first and second natural frequencies. The relative tangential motion (which is also the slip displacement) is shown in (a), (b), and (c) for the left, center, and right regions, respectively. The relative normal motion (which is also the separation displacement) is shown in (d), (e), and (f) for the left, center, and right regions, respectively. The shaded area is where the bolts are located.

essary to initiate slip are higher too. Thus the contact stiffness for the CG configuration is the highest of the three, and the dissipation characteristics are the lowest.

According to Table 3, the linear natural frequencies for conformal cases increase with the curvature from 0 to 1000 μm but have a slight decrease for the 5000 μm curvature. In Fig. 8(a) and (b), with the increase of the curvature, the variation of the amplitude-dependent natural frequencies increases. For 5000 μm curvature, the variation of the first natural frequency is over 4%. In Fig. 8(c) and (d), the damping ratios show an increasing trend with curvature. After the fixed sine tests, the natural frequencies uniformly increase between 0.5 and 2.5 Hz depending on the configuration, and the damping ratios decrease between 0.03 and 0.53% at high amplitudes (but remain unchanged at low amplitudes). These results are further summarized in Table 4.

The hammer test results for the EG configurations are shown in Fig. 9. The variation of natural frequencies decreases as the curvature increases from 250 to 5000 μm in Fig. 9(a) and (b). All configurations for EG show significantly lower damping ratios than for the conformal cases other than the 0–0 flat case, and the damping ratios decrease with the curvature increasing from 250 to 5000 μm (Fig. 9(c) and (d)). Compared with the conformal configurations (including the 0-0 case), the EG configurations exhibit more linear characteristics since the natural frequencies and damping ratios change less with amplitude. Interestingly, the percent change in frequency for the first mode in the 0-0 flat case is nearly identical to that of the 0-1000 EG configuration. According to Table 3, with the increase of the curvature, the natural frequencies for the EG configurations decrease. After the fixed sine tests, the variation of the natural frequencies of all EG configurations is less than 1 Hz. The variation in the damping ratios was observed to decrease as the curvatures increased. These results are summarized in Table 4.

The hammer test results for the CG configurations are shown in Fig. 10. The variation of natural frequencies decreases with the curvature from 250 to 5000 μm (Fig. 10(a) and (b)). In Fig. 10(c) and (d), the damping ratios of the first and second mode decrease as the curvatures increase from 250 to 5000 μm. For the low amplitude properties in Table 3, the natural frequencies of the CG configurations increase for the first mode and decrease for the second mode as the curvature increases. After the fixed sine tests, the 250 μm curvature increases in natural frequencies and decreases in damping ratios; however, the high curvatures of 1000 and 5000 μm both show little variation in natural frequencies and damping ratios after the fixed sine tests. All of the changes are summarized in Table 4.

The conformal configurations exhibit the most nonlinearity of all of the structures, as the natural frequencies and damping ratios change the most (both in terms of the changes in mean values from before to after the fixed sine test and the amplitude-dependent properties). The natural frequencies and damping ratios for the EG configurations decrease with the

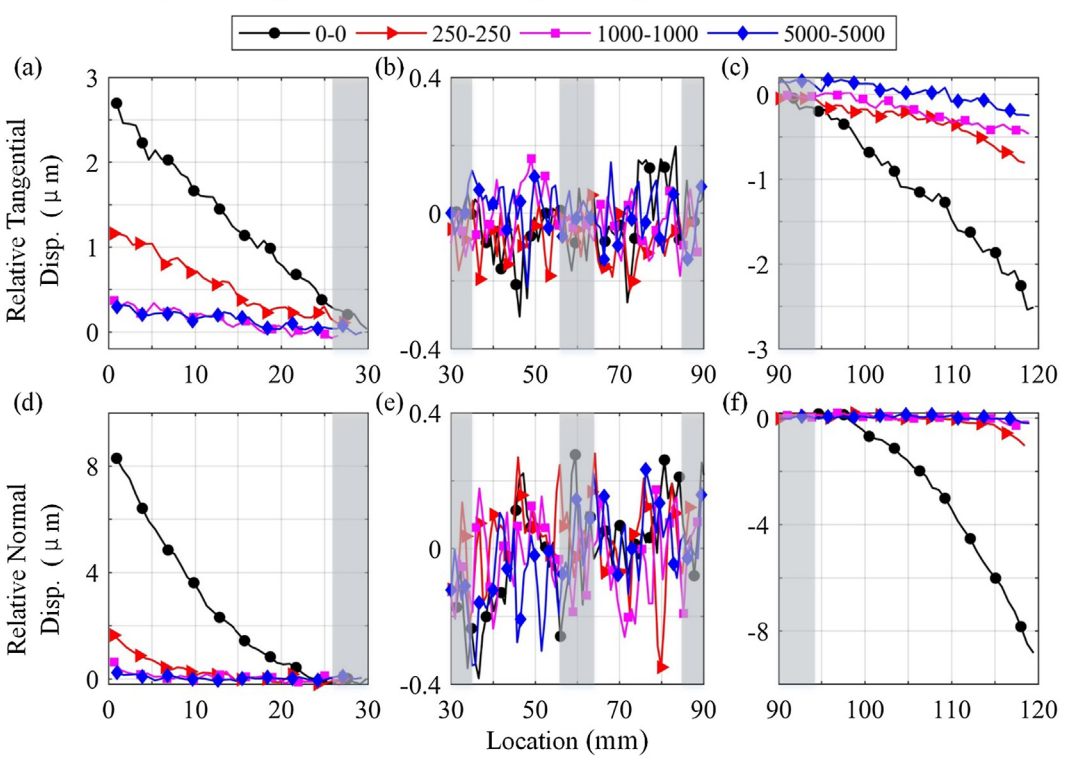

Fig. 14. The relative tangential and normal displacements of the interfaces for the conformal configurations with a 5 N sinusoid at the first natural frequency. Shown are the slip behavior of the interface in the (a) left, (b) center and (c) right regions, and the separation behavior in the (d) left, (e) center and (f) right regions.

increase of the curvatures. Therefore, the EG configurations decrease the stiffness and damping of the systems as the curvature is increased. The CG configurations increase the stiffness but decrease the damping of the systems compared to the conformal systems. The change of natural frequencies and damping ratios from before to after the fixed sine tests implies that more wear occurs for the interfaces with large contact areas since the natural frequencies and damping ratios show relatively large changes for the conformal configurations and the low curvature (250 μm) EG and CG configurations.

3.2. DIC analysis

3.2.1. Baseline configuration

The BRB with the flat interface is shown as an example for how the separation and slip behaviors of the interface were extracted. As described in Section 2.3, the whole interface was divided into three sub-regions to improve accuracy. In Fig. 11 (a), the X direction is along the interface and responses in this direction are the tangential motion of the interface. The responses in the Y direction are defined as the normal motion. The BRB was excited by a shaker at the first natural frequency in the Y direction with 5 N excitation amplitude. A coordinate system is defined for the interface such that it spans from 0 to 120 mm in the X direction, with the three bolts located at approximately 30, 60, and 90 mm. Fig. 11(b) shows the left region of the interface where the red and blue lines consist of approximately 45 subsets above and below the interface. The displacement responses of the red and blue lines in X and Y directions are extracted and shown in Fig. 11(c), (d), (f), and (g). To calculate the relative tangential (slip) and normal (separation) displacements, the motions in the X and Y directions, respectively, measured along the blue line are subtracted from the motions along the red line, as shown in Fig. 11(e) and (h). Since the excitation is a steady sinusoid, the amplitudes of the subsets in the red and blue lines are repeatedly measured across multiple periods of the response. The amplitude of the red line, the amplitude of the blue line, and their difference in the X and Y directions are shown in Fig. 12.

As shown in Fig. 12, the amplitude of the normal motion (more than 140 μm) is much larger than that of the tangential motion (less than 5 μm) of the interface. At the location coordinate of 0 mm, the amplitudes of slip and separation reach the maximum levels of 2.7 and 8.2 μm, respectively. The slip and separation behaviors both decrease to zero when approaching the bolted portion of the interface.

The procedure to extract the relative normal (separation) and tangential (slip) motions in the interface is next applied to each of the other systems for multiple excitation levels and modes. Fig. 13 shows how the normal and tangential behavior change with excitation frequency and amplitude.

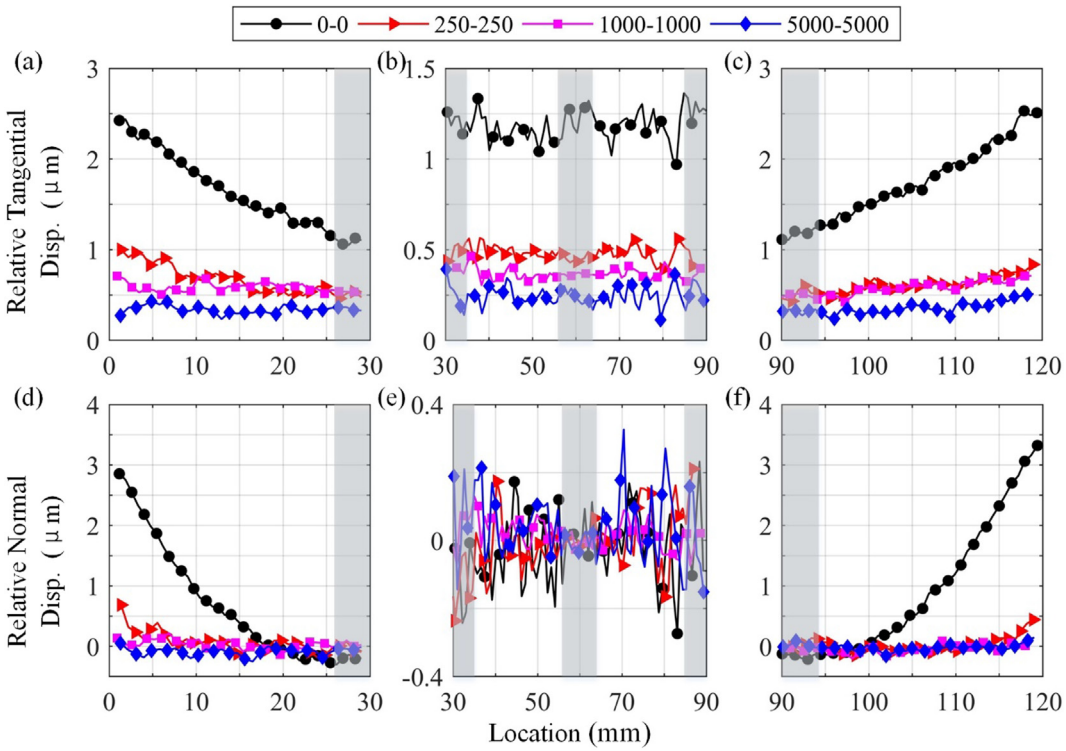

Fig. 15. The relative tangential and normal displacements of the interfaces for the conformal configurations with a 5 N sinusoid at the second natural frequency. Shown are the slip behavior of the interface in the (a) left, (b) center and (c) right regions, and the separation behavior in the (d) left, (e) center and (f) right regions.

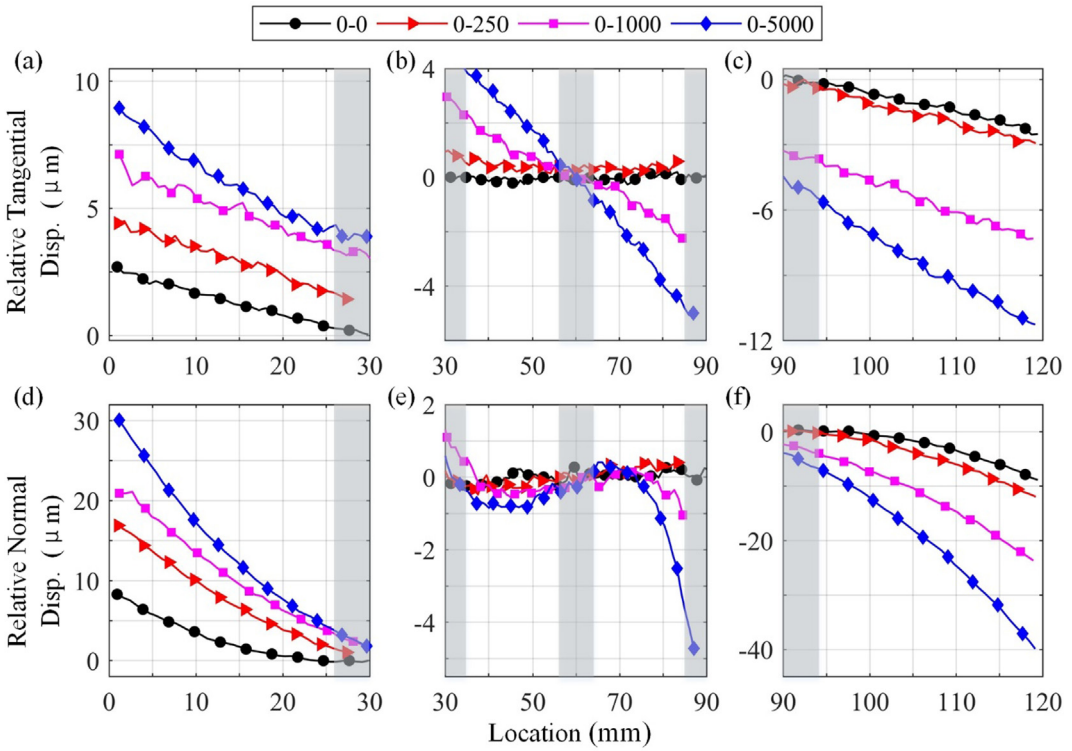

Fig. 16. The relative tangential and normal displacements of the interfaces for the EG configurations with a 5 N sinusoid at the first natural frequency. Shown are the relative tangential motions of the interface in the (a) left, (b) center, and (c) right regions, and the relative normal motions in the (d) left, (e) center, and (f) right regions.

In Fig. 13, the amplitude of slip and separation behaviors does not show a linear relationship with the excitation level since the amplitudes of slip and separation for the 5 N case are at most, only 60% greater than those for the 2 N case. The noisy responses shown in Fig. 13(e) are indicative of the minimum resolution in measurements achieved with this specific test setup (0.23 μm). For the separation behaviors in Fig. 13(d)–(f), the first and the second modes show the same trend, but with the amplitudes of the first mode approximately twice of that of the second mode. For the slip behaviors in Fig. 13(a)–(c), the first mode transits from slipping in the positive direction on one side of the interface to slipping in the opposite direction on the other side of the interface. This behavior is consistent with the mode shape of the first mode, which has a peak modal displacement in the center of the interface (i.e. that of a free-free beam bending in the first mode). The second mode, however, shows slip in the same direction across the entire interface, with a slip of 1.2 μm in the center region for the 5 N case. Therefore, for both 2 and 5 N excitations, the second mode exhibits macroslip during fixed sine excitation.

3.2.2. Conformal configuration

In the previous section, the special case of conformal configuration (here, referred to as flat or the 0-0 case), in which the macroscale curvature of the interface was negligible, was analyzed. Fig. 14 shows the response of the conformal configurations spanning from the 0-0 case to the 5000-5000 case for the first natural frequency. As the radius of curvature of the interface increases, both the relative normal (separation) and tangential (slip) displacements of the interface decrease. The separation behavior transits from large displacements at the edge of the interface to almost zero displacement for small increases in curvature (for the 250-250 case, the displacement decreased by 75% from the 0-0 case, and the 5000-5000 case has approximately no displacement as shown in Fig. 14(d) and (f)). By comparison, the slip behavior decreases by 55% from the 0-0 case to the 250-250 case, and the larger curvatures exhibit non-zero slip still (Fig. 14(a) and (c)). For the first mode (Fig. 14(b) and (e)), both the normal and tangential displacements are negligible across the center region. For the largest curvature tested (5000-5000), both the normal and tangential displacements trend towards zero across the entire interface.

A similar trend to the first mode is observed for the second mode in Fig. 15. The relative tangential and normal motions both decrease with the increase of the curvature. Similar to the flat curvature in Fig. 13, both sides of the interface exhibit slip and separation in the same direction. The slip behaviors for all configurations are in the same direction and not zero across the interface. For the high curvature conformal configuration, the 5000-5000 case has approximately zero separation along the interface. This implies that the local kinematics for the normal direction of an interface, can be suppressed (or neglected) if there is suitably high curvature (though the contact pressure may still vary). It remains to be seen, however, if this trend

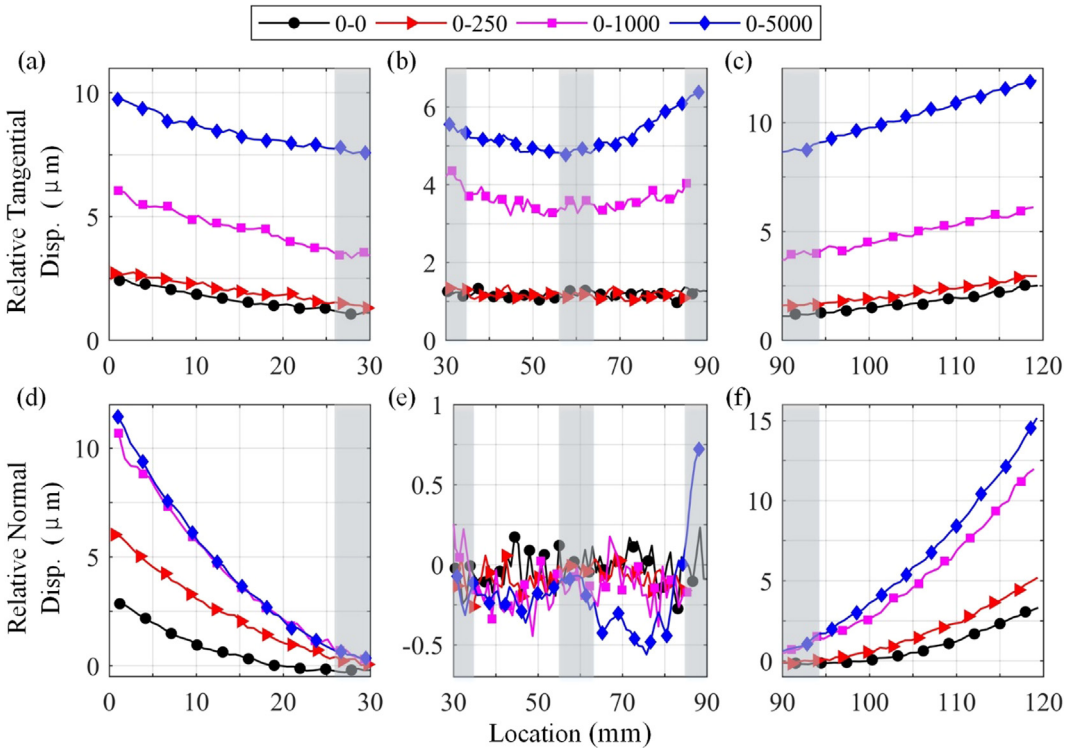

Fig. 17. The relative tangential and normal displacements of the interfaces of the EG configurations with a 5 N sinusoid at the second natural frequency. Shown are the relative tangential motions of the interface in the (a) left, (b) center, and (c) right regions, and the relative normal motions in the (d) left, (e) center, and (f) right regions.

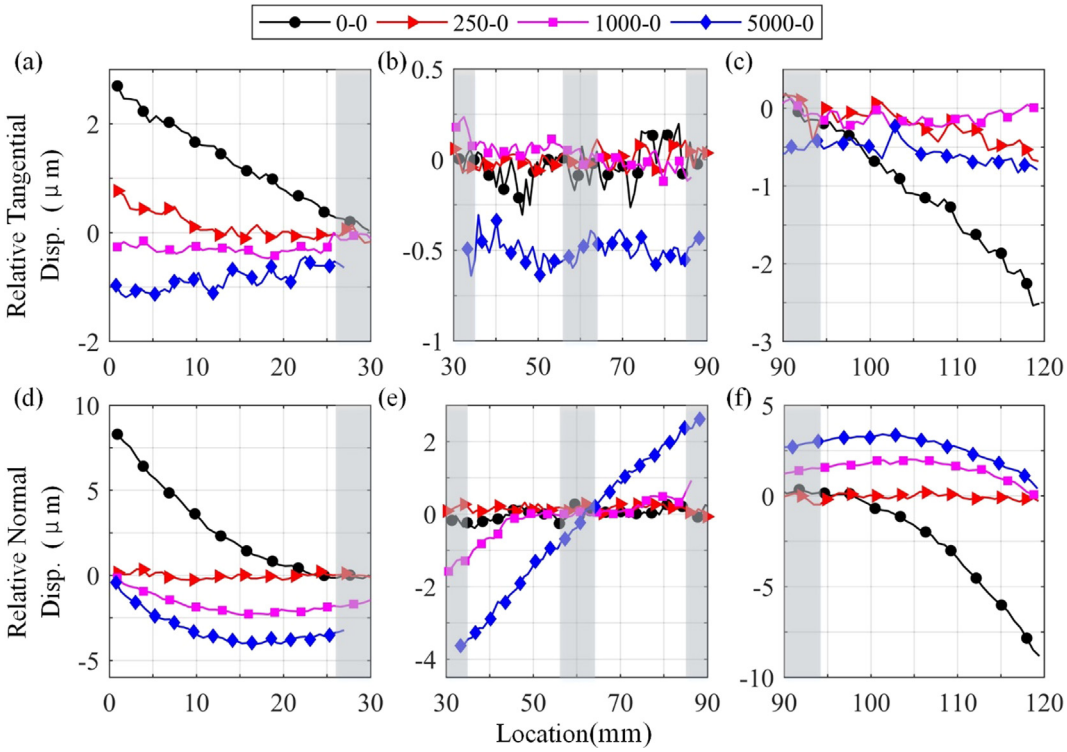

Fig. 18. The relative tangential and normal displacements of the interfaces of the CG configurations with a 5 N sinusoid at the first natural frequency. Shown are the relative tangential motions of the interface in the (a) left, (b) center, and (c) right regions, and the relative normal motions in the (d) left, (e) center, and (f) right regions.

persists across higher modes. At the same time, the slip behavior becomes small as the interface curvature is increased; however, as the work done by frictional forces scales with displacement multiplied by contact pressure (in a Coulombic model [8]), it is not possible to say from this study alone if the local kinematics for the tangential direction of an interface can be ignored if the curvature is sufficiently large. Even if there is a small amount of slip, this could still result in large amounts of frictional dissipation.

3.2.3. Edge gap configuration

The next configuration studied is the EG. In this configuration, there is no contact in the outer region of the interface for high curvature cases (thus, the displacements do not indicate slip and separation but rather relative tangential and normal motions in these area). Fig. 16 shows that, compared to the conformal configurations shown in Fig. 14, there is more relative tangential and normal displacement at the left and right bolt locations. The magnitude of displacement in the left and right regions is significantly higher than for the conformal configurations, which makes sense given that the edges of the beams are out of contact.

For the second mode, macroslip is observed for all configurations (Fig. 17). As the curvature increases, the magnitude of macroslip is observed to increase to 5 μm for the 0-5000 case, as shown in Fig. 17(b). The relative normal displacement also increases with curvature, though not as dramatically as for the first mode (Fig. 16). Of note, the response is asymmetric: more relative tangential and normal displacement is observed on the right side of the interface than the left side of the interface. This is possibly due to the location of the shaker's attachment point being to the left of the beam, and future experiments should seek to address this.

3.2.4. Center gap configuration

The last configuration studied is the CG. In this configuration, there is no contact in the center region of the interface for high curvature cases (thus, the displacements do not indicate slip and separation but rather relative tangential and normal motions). For the relative tangential motions in Fig. 18(a), the slip behavior (i.e., displacements at 0 and 120 mm) transits from being in opposite direction for the 250-0 case to no appreciable slip for the 1000-0 case to slip in the same direction for the 5000-0 case (Fig. 18(a) and (c)). This indicates that for the 250-0 and 1000-0 cases, microslip is observed, but for the 5000-0 case, macroslip is observed (as the center region is not in contact for this configuration). In Fig. 18(d)–(f), with the increase of curvature, the relative normal motions of the CG configurations decrease to approximately zero across the entire interface for the 250 μm curvature and then increase in the opposite direction for high curvature configurations. The contact

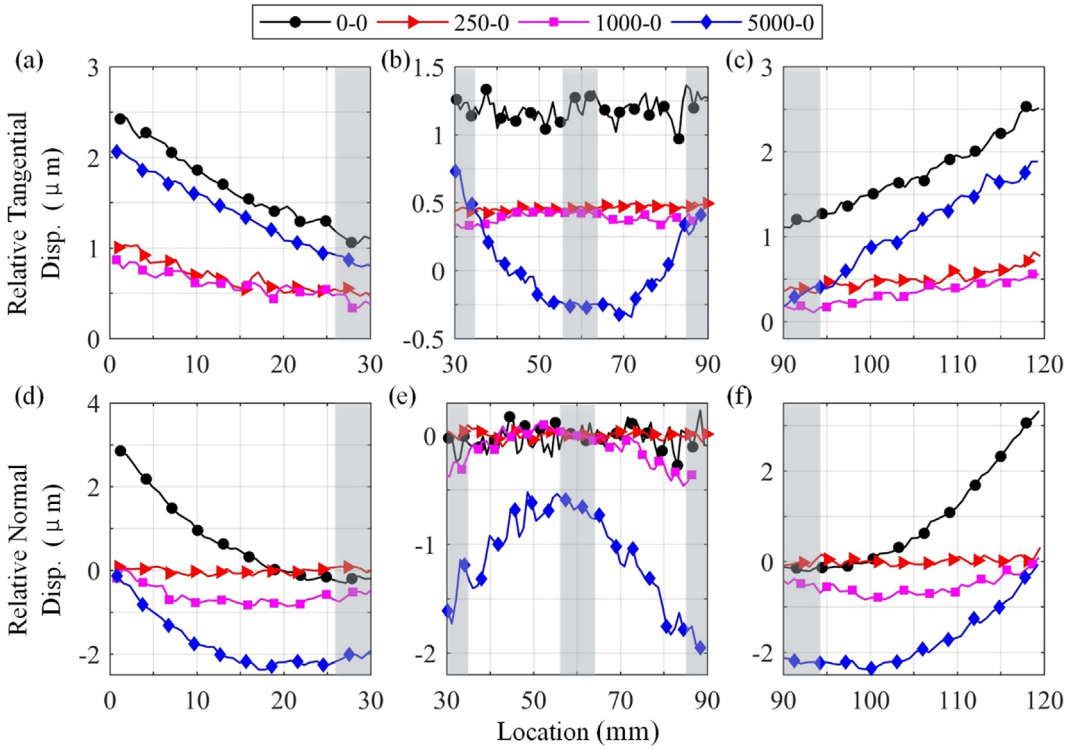

Fig. 19. The relative tangential and normal displacements of the interfaces of the CG configurations with a 5 N sinusoid at the second natural frequency. Shown are the relative tangential motions of the interface in the (a) left, (b) center, and (c) right regions, and the relative normal motions in the (d) left, (e) center, and (f) right regions.

areas for the 1000 and 5000 μm curvatures are the two edges of the interface (at 0 and 120 mm), where there are no relative normal motions. By contrast, the 250 μm curvature case is in contact along the entire length of the interface as the preload is sufficiently large to close the gap between the two beams. However, no normal displacement is observed along the entire length of the 250-0 case. Therefore, no separation behaviors happen for any of the CG configurations.

For the second mode, macroslip is observed for all configurations in Fig. 19(a)–(c). It should be noted that there are relative tangential motions in the same direction at the contact areas (0 and 120 mm) for the 5000-0 configuration (Fig. 19(a) and (c)) that are significantly larger than for small curvatures. For the relative normal motions in Fig. 19(d)–(f), with the increase of curvature, the amplitudes decrease to no appreciable displacements for the 250 μm curvature and then increase in the opposite direction for the 1000 and 5000 μm curvatures. Similar to the results of the first mode, there are no separation behaviors for the CG configurations since no relative normal motions occur at the contact areas.

3.2.5. Comparison of all configurations

To investigate the effect of the conformal, the EG, and the CG configurations, the 5000 μm curvature cases for each configuration are discussed in the following. First, the nonlinear characteristics of the conformal, EG, and CG configurations are summarized in Fig. 20, which shows the hammer test results for the 5000 μm curvature cases and the reference flat case. The 5000-5000 conformal case exhibits the most nonlinearity of all of the configurations since the natural frequency and damping ratio both for the first and second modes show the largest change. The EG and CG configurations (0-5000 and 5000-0, respectively) both show small changes in natural frequencies and damping ratios. This is consistent with previous studies of a similar system [25]: interfaces designed to have Hertzian contact (similar to the EG configuration) and interfaces designed to have only small contact patches with high contact pressures (similar to the CG configurations) were found to achieve more linear characteristics than flat interfaces.

The observations of the nonlinear characteristics are complemented by the measurements of the relative tangential and normal displacements of the 5000 curvature cases in the different configurations and the reference flat interface, which are shown in Fig. 21 for the first mode. Compared to the other configurations, the conformal configuration 5000-5000 has the least separation and slip, while the EG configuration has the largest normal and tangential displacements. By contrast, the 5000-0 CG case shows macroslip behavior and no separation behaviors at the contact areas (0 and 120 mm).

For the second mode (Fig. 22), a similar trend as the first mode is observed: the EG configuration (0-5000) has the largest relative tangential and normal motion in the left and right regions. However, the conformal configuration (5000-5000) has

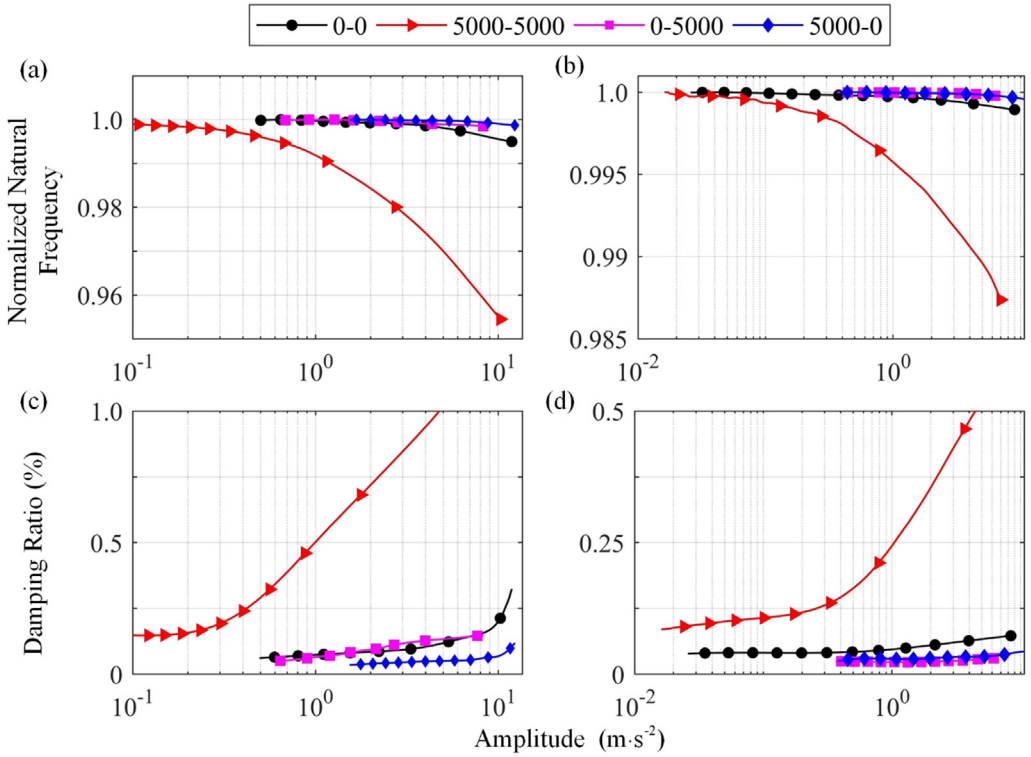

Fig. 20. The amplitude-dependent natural frequencies and damping ratios for the first and second modes of the flat (0-0) case, 5000-5000 conformal case, the 0-5000 EG case, and the 5000-0 CG case from the hammer tests of 500 N. The normalized natural frequencies for (a) the first and (b) second modes are shown, and the amplitude-dependent damping ratios for (c) the first and (d) second modes are shown.

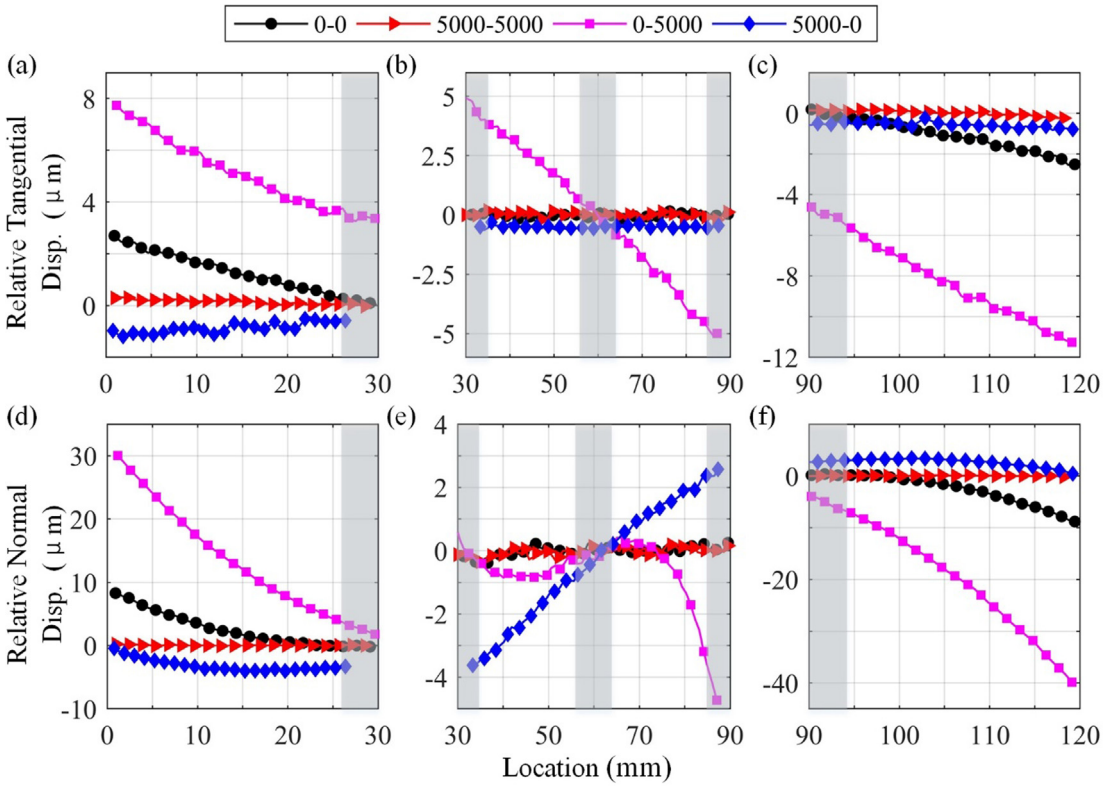

Fig. 21. Comparison of relative tangential and normal displacements for the interfaces of the flat configuration and all of the 5000 curvature configurations excited by a 5 N sinusoid at the first natural frequency. Shown are the relative tangential motions of the interface in the (a) left, (b) center, and (c) right regions, and the relative normal motions in the (d) left, (e) center, and (f) right regions.

negligible separation along the interface. The CG configuration (5000-0) has no separation at the contact area and has a normal displacement response that is 180°out of phase with respect to all other configurations. All configurations exhibit macroslip behavior during excitation at the second natural frequency of each system, though the measured slip for the 5000-5000 configuration is only 80% larger than the noise floor of the measurements.

4. Discussion

The major results of this paper demonstrate that there are non-zero slip (both micro- and macro-slip) and separation in the jointed interfaces studied. Thus, in order to model a similar jointed structure accurately, these results imply that it is paramount to include the local kinematics (both in the normal and tangential directions of a joint). This consequence is at odds with many traditional joint models. For instance, the traditional approach to modeling a joint with Iwan elements [2,7,10] regularizes the contact interface by tying a large number of nodes on the contact surface to a single, fictitious node that is then connected to a single, fictitious node on the opposite surface via an Iwan element. This regularization assumes no local kinematics - all points on the surface that are tied to the Iwan element have the same displacement (or some other non-physical assumed distribution). Other, similar whole joint modeling approaches, such as the use of Bouc-Wen friction models or other hysteretic models designed to represent the dissipation of a jointed structure [1], have a similar challenge in that they preserve the hysteretic behavior of a system while neglecting the local kinematics.

The alternative approach is to model an interface in high fidelity with node-to-node contact (in which either Coulomb or Jenkins models are commonly used [1]). However, the friction models used in this approach, traditionally, have been unable to capture the hysteretic behavior of the jointed structure accurately without herculean efforts (e.g., [2]). Thus, while it is important to preserve the local kinematics as shown by this study, it is also important to represent the frictional dissipation of a surface accurately, which is an ongoing research challenge.

In investigating the role of contact geometry on the dynamics and local kinematics of the jointed structure studied, many of the results are in accordance with what might be predicted by contact mechanics [38,39]. The CG configuration relegates contact to two sharp edges, which leads to high contact forces and no separation. Due to the high contact forces, the slip amplitude is much smaller for the CG configuration than for either the flat or the EG configurations. Likewise, the conformal configuration, which is similar to pin-in-hole contact, is much stiffer than either the EG or flat configuration as would be predicted via contact mechanics. The EG configuration is similar to Hertzian contact where one surface is able to be described by a

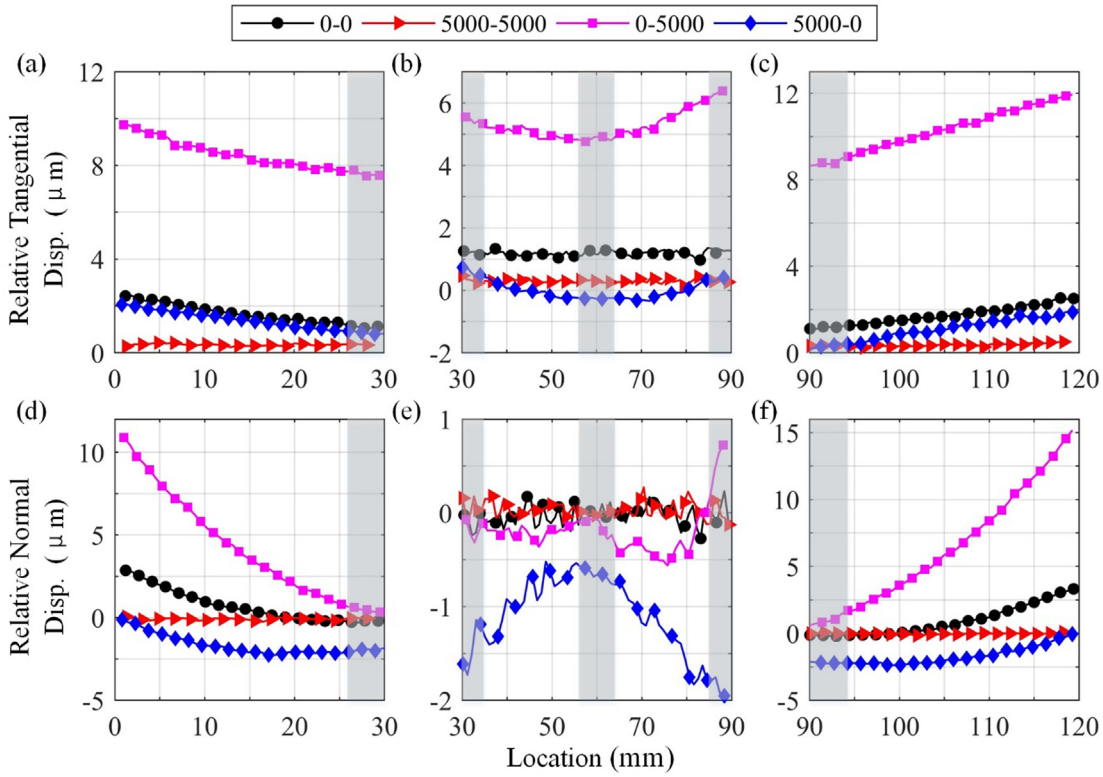

Fig. 22. Comparison of the relative tangential and normal motions for the interfaces of the flat configuration and all of the 5000 curvature configurations excited by a 5 N sinusoid at the second natural frequency. Shown are the relative tangential motions of the interfaces in the (a) left, (b) center, and (c) right regions, and the relative normal motions in the (d) left, (e) center, and (f) right regions.

parabola, and the other is flat. Contact mechanics theory indicates that the load for Hertzian contact is related directly to the contact area. As the interface is dynamically loaded in the present study, the contact area is observed to change accordingly.

The response of the conformal configuration is particularly interesting. In terms of the nonlinear dynamic properties, the conformal system exhibits the strongest nonlinearity. However, in terms of slip and separation, the conformal system shows the smallest amount of tangential motion (slip in this case) and negligible separation for both mode 1 and mode 2. This paradox, that the system with the most nonlinear behavior has the least amount of motion at the contact interface, is partly explained by the conformal system having the greatest contact area of all of the systems studied. Even though there are only small tangential displacements, these could result in the largest frictional forces due to the high contact area that the forces are acting on. Further, in terms of the natural frequencies, the expression of the nonlinearity is observed to be related to the amount of contact area for each system. The strongest nonlinearity is observed for the conformal system, then the flat interface, and the weakest nonlinearity is observed for the CG configuration (which has the smallest contact area). Further investigation to confirm and explore these results is warranted, such as by studying the contact pressures (e.g., the technique of [20,21,40]) or by investigating the local kinematics on the interior of the interface (which cannot be measured via DIC, but could be adequately studied by computational methods).

5. Summary and conclusions

In this research, DIC is used to visualize the local kinematic behaviors of a jointed interface. In order to develop physical insights into the dynamics of a real interface, the influence of the interfacial curvature on slip and separation behavior is studied. This research experimentally verified that the contact patches of lap joints significantly change during the dynamic excitation. For instance, the interfaces exhibit clapping behavior during the steady sinusoidal excitation. The distribution of slip behavior along the entire interface is also extracted, and the effect of the interface curvature on both separation and slip are studied in detail.

Specific findings from this research are:

DIC for joint dynamics: The DIC method is able to measurement the local kinematic behavior of the interface with high spatial resolution. In the verification experiment, the DIC measurement is compared with other well-developed measurement methods and found to have an accuracy of 0.23 μm for this experimental setup.

Effect of curvature on nonlinearity: The conformal configurations exhibit the most nonlinearity of all of the structures, as the amplitude-dependent natural frequencies and damping ratios change the most. In addition, with the increase of the curvature, the change of the amplitude-dependent properties increases, though the edge gap and center gap configurations show less change in the amplitude-dependent properties than the conformal configurations.

The kinematic behavior of the conformal configurations: For the conformal configurations, the slip and separation behaviors both decrease as the curvature increases and, compared with the slip behavior, the separation behavior decreases dramatically. This implies that the local kinematics of an interface for the conformal configuration, especially the separation behavior, can be suppressed (or neglected) if there is suitably high curvature. At the same time, it is hypothesized that with the reduction in measured relative normal and tangential motions, the contact pressure in the interface increases. Future work must test this notion, such as in [20,40].

The kinematic behavior of the edge gap configurations: For the edge gap configurations, the relative tangential and normal motions increase with the curvature of the interface. The edge gap configurations for the joints commonly decrease the stiffness of the whole system (from the hammer test results). With less stiffness at the joints, the interfaces show larger relative normal and tangential displacements.

The kinematic behavior of the center gap configurations: With the increase of the curvature, the relative normal motions of the center gap configurations decrease to no appreciable level for 250 μm curvature and then increase in the opposite direction for the higher curvatures. For all center gap configurations, there are no separations at the interface. The relative tangential motion also shows a decreasing and then increasing magnitude with the increase of the curvature, with the lowest level occurring for the 1000 μm curvature.

The macroslip behavior: In the first mode of the BRB systems, microslip is observed at the contact patch, where the edges of the contact have a large relative tangential motion (slip) compared to the bolted portion. For the second mode of all the test specimens, macroslip is observed for a 5 N excitation. This is in direct contradiction to prior modeling assumptions and demonstrates that the slip behavior is strongly affected by the excitation frequency, mode shape, and location of the joint within a structure.

Low amplitude natural frequencies and damping ratios: For the high curvature configurations, the conformal and center gap configurations increase the stiffness of the joint, while the edge gap configuration decreases the stiffness. At the same time, the conformal configuration has the largest damping ratio and shows an increasing trend with the curvature. However, the edge gap and center gap configuration both decrease the damping ratio compared with the flat interface.

Wear: As indirectly measured by comparing the nonlinear properties of each system both before and after shaker testing, the configurations with more contact area (the conformal configurations and the low curvature (250 μm) edge gap and center gap configurations) tend to have larger changes in the natural frequency and damping ratios, thus exhibiting more wear. Future work is needed to rigorously quantify this thought.

Acknowledgement

The first author wants to thank China Scholarship Council (CSC) for financial support in Rice University. The authors would like to thank Scott Smith for his assistance in the experimental setup.

References

[1] M.R.W. Brake, The Mechanics of Jointed Structures: Recent Research and Open Challenges for Developing Predictive Models for Structural Dynamics, Springer, Cham, Switzerland, 2017.
[2] R.M. Lacayo, L. Pesaresi, J. Groß, D. Fochler, J. Armand, L. Salles, C.W. Schwingshackl, M.S. Allen, M.R.W. Brake, Nonlinear modeling of structures with bolted joints: a comparison of two approaches based on a time-domain and frequency-domain solver, Mech. Syst. Signal Process. 114 (2019) 413–438.
[3] Y. Luan, Z. Guan, G. Cheng, S. Liu, A simplified nonlinear dynamic model for the analysis of pipe structures with bolted flange joints, J. Sound Vib. 331 (2) (2012) 325–344.
[4] C.W. Schwingshackl, D. Di Maio, I. Sever, J.S. Green, Modeling and validation of the nonlinear dynamic behavior of bolted flange joints, J. Eng. Gas Turbines Power 135 (12) (2013), 122504–122504-8.
[5] E.P. Petrov, A high-accuracy model reduction for analysis of nonlinear vibrations in structures with contact interfaces, J. Eng. Gas Turbines Power 133 (10) (2011), 102503–102503-10.
[6] C.W. Schwingshackl, E.P. Petrov, D.J. Ewins, Measured and estimated friction interface parameters in a nonlinear dynamic analysis, Mech. Syst. Signal Process. 28 (2012) 574–584.
[7] N.N. Balaji, M.R.W. Brake, The surrogate system hypothesis for joint mechanics, Mech. Syst. Signal Process. 126 (2019) 42–64.
[8] L. Gaul, R. Nitsche, The role of friction in mechanical joints, Appl. Mech. Rev. 54 (2) (2001) 93–106.
[9] D.J. Ewins, Exciting vibrations: the role of testing in an era of supercomputers and uncertainties, Meccanica 51 (12) (2016) 3241–3258.
[10] D.J. Segalman, D.L. Gregory, M.J. Starr, B.R. Resor, M.D. Jew, J.P. Lauffer, N.M. Ames, Handbook on dynamics of jointed structures, Sandia National Laboratories, Report No. SAND2009-4164, (2009).
[11] D.J. Segalman, A four-parameter Iwan model for lap-type joints, J. Appl. Mech. 72 (5) (2005) 752–760.
[12] D.J. Segalman, A modal approach to modeling spatially distributed vibration energy dissipation, Sandia National Laboratories, Report No. SAND2010-4763, (2010).
[13] B.J. Deaner, M.S. Allen, M.J. Starr, D.J. Segalman, H. Sumali, Application of viscous and Iwan modal damping models to experimental measurements from bolted structures, J. Vib. Acoust. 137 (2) (2015), 021012–021012-12.
[14] S. Bograd, P. Reuss, A. Schmidt, L. Gaul, M. Mayer, Modeling the dynamics of mechanical joints, Mech. Syst. Signal Process. 25 (8) (2011) 2801–2826.
[15] D. Süß, K. Willner, Investigation of a jointed friction oscillator using the Multiharmonic Balance Method, Mech. Syst. Signal Process. 52–53 (2015) 73–87.
[16] M.H. Mayer, L. Gaul, Segment-to-segment contact elements for modelling joint interfaces in finite element analysis, Mech. Syst. Signal Process. 21 (2) (2007) 724–734.

[17] T. Dreher, N.N. Balaji, J. Groß, M.R.W. Brake, M. Krack, Gerrymandering for interfaces: modeling the mechanics of jointed structures, IMAC XXXVII A Conference and Exposition on Structural Dynamics, Orlando, FL, February, 2019.
[18] Y.S. Lee, F. Nucera, A.F. Vakakis, D.M. McFarland, L.A. Bergman, Periodic orbits, damped transitions and targeted energy transfers in oscillators with vibro-impact attachments, Physica D 238 (18) (2009) 1868–1896.
[19] R.C. Flicek, K.J. Moore, G.M. Castelluccio, C. Hammetter, M.R.W. Brake, Stress waves propagating through jointed connections, IMAC XXXIV A Conference and Exposition on Structural Dynamics, Orlando, FL, January, 2016.
[20] M.R.W. Brake, J.G. Stark, S.A. Smith, D.P.T. Lancereau, T.W. Jerome, T. Dossogne, In situ measurements of contact pressure for jointed interfaces during dynamic loading experiments, IMAC XXXV A Conference and Exposition on Structural Dynamics, Garden Grove, CA, January, 2017.
[21] B. Seeger, P. Butaud, M.V. Baloglu, F. Du, M.R.W. Brake, C.W. Schwingshackl, In situ measurements of interfacial contact pressure during impact hammer tests, IMAC XXXVI A Conference and Exposition on Structural Dynamics, Orlando, FL, February, 2018.
[22] M.N. Helfrick, C. Niezrecki, P. Avitabile, T. Schmidt, 3D digital image correlation methods for full-field vibration measurement, Mech. Syst. Signal Process. 25 (3) (2011) 917–927.
[23] S.W.B. Klaassen, M. Brøns, G. Chauda, T.A. Kasper, C.W. Schwingshackl, M.R.W. Brake, Optical full field monitoring of bolted lap-joint behaviour under vibration, IMAC XXXVII A Conference and Exposition on Structural Dynamics, Orlando, FL, January, 2019.
[24] R.M. Lacayo, L. Pesaresi, D. Fochler, J. Gross, M. Brake, C. Schwingshackl, A numerical round robin to predict the dynamics of an experimentally-measured Brake-Reuss beam, IMAC XXXV A Conference and Exposition on Structural Dynamics, Garden Grove, CA, January, 2017.
[25] M.R.W. Brake, C.W. Schwingshackl, P. Reuß, Observations of variability and repeatability in jointed structures, Mech. Syst. Sig. Process. 129 (2019) 282–307.
[26] I. Lawal, S. Shah, M. Gonzalez-Madrid, T. Hu, C.W. Schwingshackl, M.R.W. Brake, The effect of non-flat interfaces on system dynamics, IMAC XXXVI A Conference and Exposition on Structural Dynamics, Orlando, FL, February, 2018.
[27] T. Dossogne, T.W. Jerome, D.P.T. Lancereau, S.A. Smith, M.R.W. Brake, B.R. Pacini, P. Reuss, C.W. Schwingshackl, Experimental assessment of jointed configuration, IMAC XXXV A Conference and Exposition on Structural Dynamics, Garden Grove, CA, January, 2017.
[28] H. Goyder, Signal processing methods for determining the properties of bolted joints, ASME 2015 International Design Engineering Technical Conferences and Computers and Information in Engineering Conference, Boston, MA, August, 2015.
[29] M. Jin, M.R.W. Brake, H. Song, Comparison of nonlinear system identification methods for free decay measurements with application to jointed structures, J. Sound Vib. 453 (4) (2019) 268–293.
[30] H. Sumali, R.A. Kellogg, Calculating Damping from Ring-Down Using Hilbert Transform and Curve Fitting, Sandia National Laboratories, Report No. SAND2011-1960C, (2011).
[31] M.W. Sracic, M.S. Allen, H. Sumali, Identifying the modal properties of nonlinear structures using measured free response time histories from a scanning laser Doppler vibrometer, Topics in Nonlinear Dynamics, vol. 3, Springer, New York, NY, 2012, pp. 269–286.
[32] B. Pan, K. Qian, H. Xie, A. Asundi, Two-dimensional digital image correlation for in-plane displacement and strain measurement: a review, Meas. Sci. Technol. 20 (6) (2009) 062001.
[33] P.L. Reu, D.P. Rohe, L.D. Jacobs, Comparison of DIC and LDV for practical vibration and modal measurements, Mech. Syst. Signal Process. 86 (2017) 2–16.
[34] P.L. Reu, E. Toussaint, E. Jones, H.A. Bruck, M. Iadicola, R. Balcaen, D.Z. Turner, T. Siebert, P. Lava, M. Simonsen, D.I.C. Challenge, Developing images and guidelines for evaluating accuracy and resolution of 2D analyses, Exp. Mech. 58 (7) (2018) 1067–1099.
[35] D.Z. Turner, Digital image correlation engine (DICe) reference manual, Sandia National Laboratories, Report No. SAND2015-10606 O, (2015).
[36] S. Yaofeng, J.H.L. Pang, Study of optimal subset size in digital image correlation of speckle pattern images, Opt. Lasers Eng. 45 (9) (2007) 967–974.
[37] P. Reu, Introduction to digital image correlation: best practices and applications, Exp. Tech. 36 (1) (2012) 3–4.
[38] K.L. Johnson, Contact Mechanics, Cambridge University Press, Cambridge, UK, 1985.
[39] J.R. Barber, Contact Mechanics, Springer, 2018.
[40] T. Dreher, Experimental and Numerical Analysis of Friction Damping in Jointed Structures: Towards a More Physics-based Approach for Interface Model Order Reduction, University of Stuttgart, Germany, 2019.